Temperature and skin-friction maps on a lifting hydrofoil in a propeller wake

M Miozzi[1] & **M Costantini**[2]

[1]National Research Council, Institute of Marine Engineering (CNR-INM), Via di Vallerano, 139, 00128 Rome, Italy
[2]German Aerospace Center (DLR), Institute of Aerodynamics and Flow Technology, Bunsenstrasse 10, 37073 Göttingen, Germany

E-mail: `massimo.miozzi@cnr.it`

July 2021

Abstract. There are at least two direct links between the friction acting on the surface of a (slightly warmer or colder) body under the influence of an incompressible flow and the temperature distribution on the surface of the body itself. The first relies on the energy equation, which connects the evolution of the temperature distribution at the wall to the action of the skin-friction field. On the other hand, the equation of passive transport of temperature perturbations at the wall unveils a direct relationship between the celerity of propagation of thermal blobs and the friction velocity. Grounding on these relationships, this paper reports about the application of different methodologies, developed to determine skin-friction fields from surface temperature maps, to the analysis of the complex flow evolution on a lifting *NACA* 0015 hydrofoil immersed in a non-uniform, unsteady wake induced by a marine propeller. The adopted temperature-sensitive paint technique allows obtaining the global temperature data with the appropriate, high resolution in space and time. The approach based on the energy equation leads to an unconventional, single-snapshots optical-flow-like methodology, which allows obtaining time-resolved, relative skin-friction fields. The two approaches based on the displacement of the wall temperature perturbations enable the determination of time- and phase-averaged, quantitative skin-friction fields. One approach grounds on a classical tracking of the thermal disturbances via optical flow, the other one relies on minimizing the discrepancy between the celerity of propagation of thermal fluctuations and the behavior expected according to the Taylor hypothesis. The analysis of the skin-friction fields obtained via the three uncorrelated, complementary approaches discloses the evolution and the mutual interaction of different flow structures (manifolds) over the hydrofoil surface at lifting and zero-lift conditions: the hub and tip vortices, the blade wake, the laminar separation bubble, and the separation at trailing edge.

1. Introduction

There are some still uncharted mechanisms underlying the complex interaction between coherent structures developing in a propeller wake and the boundary layer around a hydrofoil immersed in the wake itself. The pace imposed by the propeller spin determines the spatially non-uniform flow to cyclically evolve against the hydrofoil: the coherent structures traveling in the wake interact with the hydrofoil boundary layer, generating a complex scenario abounding of meaningful details.

We report about the interaction between the wake generated by an *INSEAN E779a* propeller and a hydrofoil model with *NACA* 0015 profile at incidence placed in its wake by using Temperature-Sensitive Paint (TSP) (for a general description of this measurement technique see Liu and Sullivan (2005) and Tropea et al. (2007)).

The *INSEAN E779a* propeller is an established benchmark for propeller studies at INM (formerly INSEAN) and in more than 80 research institutes and groups. It has been the subject of many experimental activities and a benchmark for numerical research, making it one of the most investigated propeller models (Salvatore et al., 2006, among the others). In recent years, this INM-DLR cooperative research group published a series of papers about the NACA 0015 hydrofoil, focusing on the application of Temperature-Sensitive Paint to study the flow around it (see e.g. Miozzi et al., 2019, 2020a,b). The papers report about Laminar Separation Bubble formation at different angles of attack and flow structures within it, as well as on the description of incipient stall condition and full stall onset. It represented a natural choice to join these two well-known experimental models approaching such a complex and intricate subject as the study of the flow around a rudder in a propeller wake. With this research background, the paper focuses on the characterization of the mutual interaction between the propeller wake structures and the hydrofoil boundary layer ones, as seen by the original point-of-view of the hydrofoil surface. To this aim, the skin friction is probably the most proper quantity among those available in the experimental fluid mechanics, because of its added support in the understanding of laminar and turbulent boundary-layer evolution and the investigation of flow separation and reattachment, being that knowledge a primary input for surface design and flow control and being an accurate measurement resolved in space and time still an ongoing question. The time-resolved evolution of the skin-friction vector field topology can capture the loci of flow separation and reattachment in high detail, conveying a straightforward portrait of critical points and lines on the hydrofoil surface. This paper deals with this subject with an experimental approach focused on the temporal evolution of the temperature map of the hydrofoil surface coated by a Europium-based TSP and on the skin-friction data derived from it. The resulting time history retains a detailed portrait of the footprints of the coherent flow structures acting close to the surface, under the hypothesis that the wall heat flux is mainly due to the convective action of the flow in the boundary layer (Miozzi et al., 2019). Data reported supporting this assumption include a parametric description of the surface temperature distribution at fixed propeller advance ratio $J = 0.88$ and chord-based Reynolds number $Re_C = 4.1 \times 10^5$, for increasing Angles Of Attack AoA (0°, 4° and 8°), using profiles and maps extracted from time- and phase-averaged datasets, together with a description of the skin-friction topology extracted from both dataset to characterize flow structures at the wall.

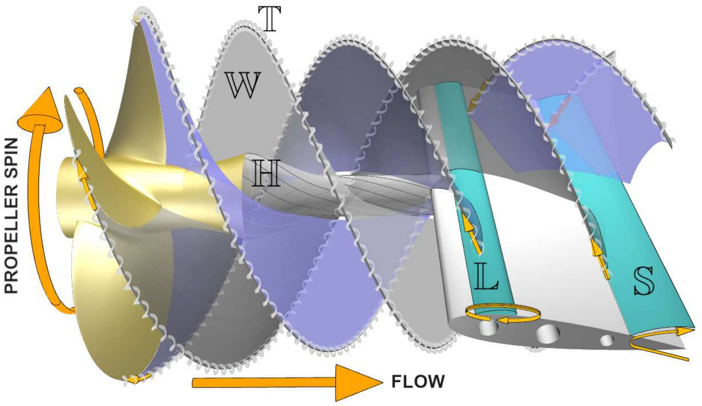

Figure 1: Conceptual scheme of the coupling between the *INSEAN E779a* propeller, equipped with a trumpet-like hub, and the hydrofoil model with *NACA* 0015 profile at $AoA = 8°$. The scheme reports vorticity manifolds raised at the propeller blades (tip $\mathbb{T}$ and trailing edge $\mathbb{W}$) and at the trumpet-shaped hub, $\mathbb{H}$, traveling in an ideal flow without the profile and similarly, the LSB $\mathbb{L}$ and trailing-edge separation $\mathbb{S}$ structures developing on the suction side as in a crossflow configuration without propeller.

The main features acting in a propeller-hydrofoil system flow summarize in a set of coherent flow structures ranked by their origin, the propeller or the hydrofoil. It is worth mentioning that while the first class of events, whose related manifolds rise on the propeller and develop in the wake, are well described in the scientific and technical literature on this subject (see e.g. Muscari et al. (2017) and Felli (2021) and references within), the second class, involving flow separation, transition, and reattachment on the hydrofoil surface, are here reported for the first time in the context of fluid dynamic interaction between a rotor wake and a hydrofoil. Despite their energetic impact on the flow topology at the wall, in particular at lifting conditions, both numerical and experimental reports lack in considering them in detail, likely because of the difficulties in resolving the small spatial and temporal scales involved in flow separation, transition, and reattachment, with the additional complexity introduced by the spatial non-uniformity induced by the propeller spin.

Figure 1 visualizes, in a taxonomic attempt, an idealized portrait of this complex scenario, i.e. propeller-originated manifolds evolving without hydrofoil and vice-versa. Such classification provides the taxonomic support adopted in this paper, useful in handling the complex scenario studied in this work, but nowise hypothesize a physics-based decoupling between phenomena, which are in continuous, mutual interaction.
On the propeller side, two helical manifolds detach from each blade tip ($\mathbb{T}$) and trailing edge ($\mathbb{W}$) and a longitudinal, streamwise-oriented one originating at the hub ($\mathbb{H}$) (see e.g. Felli (2021), Muscari et al. (2017) and Posa et al. (2020), among the others). The manifolds $\mathbb{T}$ and $\mathbb{W}$ impact almost orthogonally ($\approx 105°$, see Felli (2021)) to the mean plane as a tubular vortex and a vortex sheet, respectively. The manifold $\mathbb{H}$ travels in the mean plane of the hydrofoil model, perpendicularly to its leading edge (Figure 1).

On the side of the hydrofoil boundary layer, the adverse pressure gradient on the suction surface at the investigated AoA and Re_C induces flow separation. The separated flow undergoes a transition to turbulence, then reattaches to the wall (see Gaster (1966) and Miozzi et al. (2019), among others), giving rise to a reverse-flow structure commonly referred to as Laminar Separation Bubble (LSB, manifold $\mathbb{L}$ in Figure 1). In higher AoA configurations, the adverse pressure gradient hampers the flow to remain attached to the model surface up to the trailing edge: a further, turbulent separation occurs downstream of the LSB (manifold $\mathbb{S}$ in Figure 1). As described below, this separation occupies a restricted spatial region for few phase instants.
The complexity of the involved phenomena and their interaction, paired with the main focus concerning the illustration of the skin-friction extracting techniques, suggests heading the present paper contents towards a first glance description of all the mentioned manifolds. Later in this work, the study in deep restricts to the dynamics occurring at LSB ($\mathbb{L}$) and its interactions with propeller blade tip and wake ($\mathbb{T}$ and $\mathbb{W}$), using the experience gained from previous applications of the algorithms to the study of hydrofoil boundary layer (Miozzi et al., 2019, 2020a).

2. Experimental set-up

2.1. Water tunnel

The experiments are carried out at CNR-INM (Rome-IT), in the CEIMM cavitation tunnel (Figure 2). This structure is a Kempf & Remmers, closed-loop water tunnel with a nozzle contraction ratio of 5.96 : 1 and a square test section, having side $B = 600\ mm$ and length $L = 2.6\ m$. The maximum achievable water speed is $U_\infty = 12\ m/s$. Within the test section, the intensity of freestream turbulence is less than 2%, while the flow uniformity is less than 3% for the vertical component and 1% for the axial one (Salvatore et al., 2006). Optical access to the test section is provided by eight *Perspex* windows, two on each side of the tunnel.

2.2. Hydrofoil model

The examined model (Figure 3, left) is a hydrofoil model shaped with a symmetric *NACA 0015* profile. It is made of aluminum, coated with a TSP-functional set of layers (Capone et al., 2015) and then polished to achieve an average surface roughness $R_a = 0.034\ \mu m$, with a standard deviation $\sigma_{R_a} = 0.03\ \mu m$ along the model spanwise coordinate Y (Miozzi et al., 2019). The hydrofoil has a chord length $C = 120\ mm$ and a span width equal to the test-section side ($L = B = 600\ mm$). The corresponding aspect ratio and blockage factor are $B/C = 5$ and $C/B = 0.2$, respectively. The model is vertically mounted in the middle of the tunnel transverse side, using a system of two flanges and counter-flanges rigidly housed in the upper and lower transparent windows. The flanges are allowed to rotate around their geometric center to set the hydrofoil profile at the desired angle of attack.

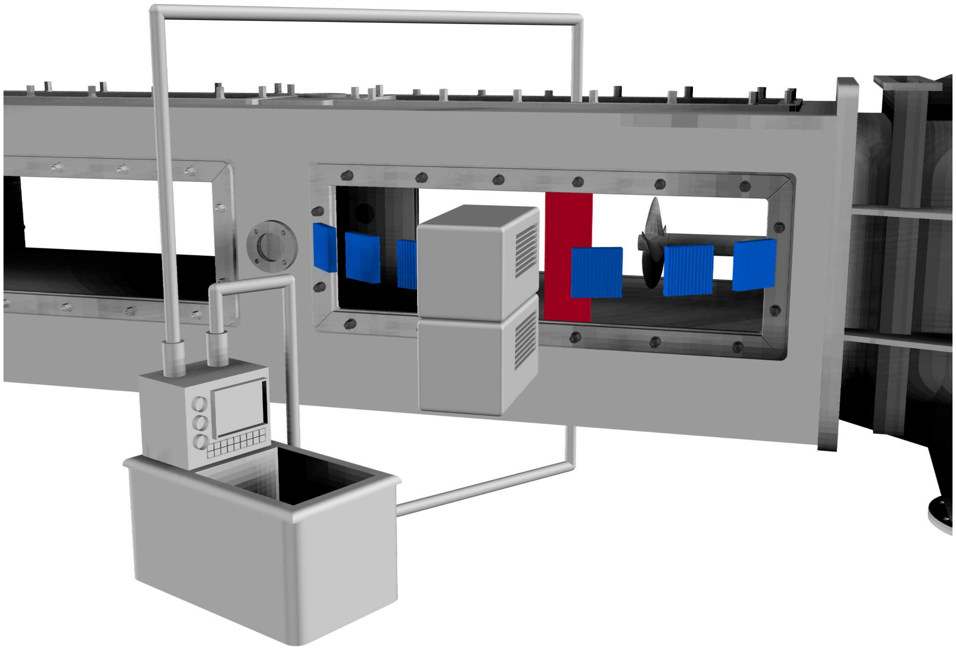

Figure 2: Conceptual scheme of the experimental setup. The flow is from the right, The *INSEAN E779a* propeller and the *NACA* 0015 profile (red) are mounted inside the test section. The LEDs (blue) illuminate the TSP-coated model surface and a couple of Photron fast cameras records the TSP emission (see Sec. 2.4.1). A pump forces heated water, warmed by an external thermostatic bath, to loop into a closed-circuit through heat exchangers, integrated in the hydrofoil model.

The body of the hydrofoil and the flanges are pierced spanwise by three ducts where heated water (warmer than the tunnel water) is forced to flow (Figure 3 left). The warm water is heated externally by means of a thermostatic bath and enables the increase of the model surface temperature above the freestream temperature, thus enhancing the signal-to-noise ratio of the thermal fingerprints of the flow structures on the model surface (see Sec. 2.4.2).
The used *Perspex* windows allow transmittance of light at both excitation and emission wavelengths (see Sec. 2.4.1), and therefore illumination and imaging from all directions (Figure 3 right).

2.3. Propeller model

The propeller involved in the present experiments is a four blades *INSEAN E779a* model (Figure 4). The model is a Wageningen modified type with fixed-pitch, right-hand and a very low skew. It has a diameter $D = 227.27\ mm$ and is mounted at a distance of $L = D/2 = 113.5\ mm$ from the hydrofoil model leading edge. The configuration adopted for the present experiment mounts a trumpet-shaped hub, whose presence muffles the

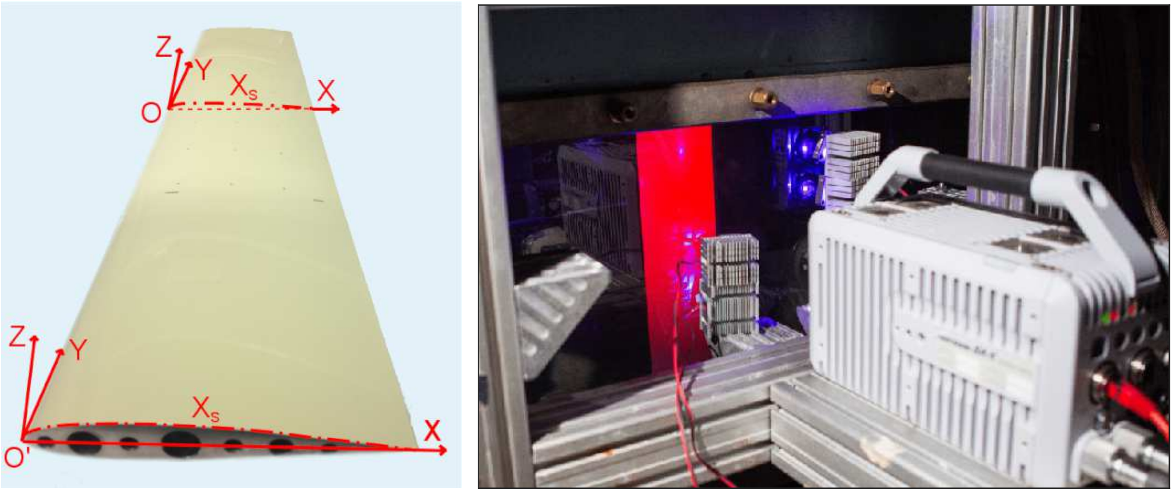

Figure 3: *NACA* 0015 hydrofoil model coated with gray-yellow TSP in natural light (left) and illuminated by the LEDs when mounted in the water tunnel (right). The red luminescence of the excited TSP is visible in the right figure.

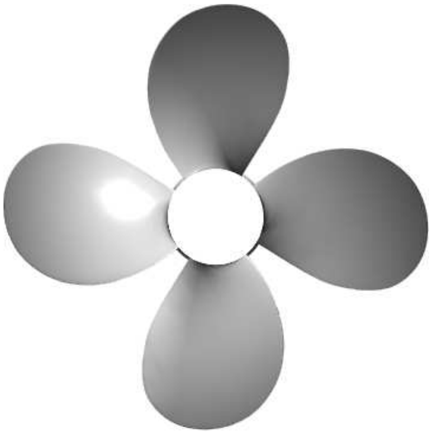

Figure 4: Sketch of the four-blades *INSEAN E779a* propeller.

INSEAN E779a model	
Diameter	$D = 227\ mm$
Number of blades	4
Pitch ratio	$P/D = 1.1$
Rake	$4°35'$ (forward)
Expanded area ratio	0.689
Hub ratio	0.200

Table 1: Main propeller parameters

importance of the associated manifold $\mathbb{H}$, thus resulting in a slight simplification of the complex mutual manifold interaction. The most relevant parameters of the propeller configuration are reported in Table 1. The Table reports propeller diameter and number of blades, together with four other propeller parameters: the pitch ratio, the rake, the expanded area ratio and the hub ratio. Further details are available in literature (see e.g. Salvatore et al., 2006, and references within).

2.4. Temperature measurement

2.4.1. TSP intensity measurements The development and the properties of the Europium-based TSP adopted in the present work are described in Ondrus et al. (2015). The same formulation was adopted in earlier works (see Capone et al. (2015), Costantini et al. (2016), Risius et al. (2018) and Costantini et al. (2019), among others). This TSP can be excited by radiations having a wavelength of about $\lambda_i = 405\ nm$. During the decay from its excited state, the TSP emits Stokes-shifted radiation at longer wavelength (peak wavelength at approximately $\lambda_e = 610\ nm$), whose intensity is tuned by the thermal quenching mechanism. This thermoluminescent phenomenon inversely links the intensity of the emission of the luminescent material to the local temperature level, modeling radiation maps featuring higher intensities at lower temperatures and vice-versa. The set of TSP-functional overlapped layers represents a high-resolution sensor in both space and time when properly observed with fast cameras mounting CCD/CMOS sensors (Charge-Coupled Device, Complementary Metal-Oxide Semiconductor) featuring adequate intensity and spatial resolution.

The investigated set-up implements the measurement principle described above by lighting the model surface with LEDs (Light-Emitting Diodes) having the peak emission close to the required wavelength of $\lambda_i = 405\ nm$. The Stokes-shifted temperature-dependent TSP emission is acquired by a couple of synchronized Photron fast cameras (SA-1.1 and SA-X2 models) at frequency $f_{acq} = 1.5\ kHz$ and shutter time $\Delta t = 1/4000s$. The cameras are equipped with CMOS sensors having 1024 square pixels resolution, 20 μm pixel size, 12 bit depth. Each camera mounts a Nikkor 50 mm f/1.4 lens, holding a long-wave pass filter having a 50% transmittance cut-point at 600 nm. The cameras are placed side-by-side just outside the lateral transparent window, at a distance from the model surface of about 350 mm (Figure 3 right). The acquired image size is fixed at $1024x752\ px$ for both cameras and the resulting Region Of Interest (ROI) is a rectangular space of $\approx 340x120\ mm$, which results in a spatial resolution of $\rho_S \approx 160\ \mu m/px$.

2.4.2. Enhancement of the Turbulent Boundary Layer signal-to-noise ratio The connection between changes in the temperature at the hydrofoil surface and the action of coherent wall-bounded flow structures (see e.g. Adrian, 2007 and Jiménez, 2018 for seminal and consolidated points of view), which displace fluid towards and away from the wall, is at the origin of the high potential inherent in using TSP to measure skin friction. During the progress of their action, the wall-bounded flow structures depict the flow topology and provide a neat description of fluid up-wash and down-wash induced by local vorticity, as well as flow separation and reattachment occurrences (Délery, 2013; Hirschel et al., 2014).

The application of a uniform heat flux across the model surface makes possible to associate a temperature distribution on the hydrofoil surface to the more or less efficient heat removal acted by the local flow, on the basis of the Fourier law $\dot{q} = h(T - T_\infty)$, where $\dot{q}$ is the heat flux, h represents the heat transfer coefficient, T is the surface temperature and T_∞ is the temperature of the freestream. It is worth to norice that in the considered incompressible flow, the temperature of the flow outside of the boundary layer is essentially the same as that of the freestream. In experiments focusing on the measurement of the laminar-turbulent transition, the popularity of TSP in detecting the transition location is related to the higher order of magnitude of the heat transfer coefficient in the turbulent boundary layer h_{turb}, compared to its laminar counterpart h_{lam}. A (small) heat flux imposed between the model surface and the surrounding flow allows the mechanical turbulent boundary layer for the random generation of colder and warmer thermal blobs, which leave their fingerprints at the model surface and propagate as passive tracers (see Miozzi et al., 2019, Figure 3 within). The measurement of the celerity of propagation of these thermal disturbances at the wall supplies a link to the celerity of propagation of velocity disturbances at the same location, and thus to the friction velocity (Miozzi et al., 2019, 2020a,b). These aspects will be discussed in Sec. 4.1.

To this aim, an external thermostatic bath forces heated water (warmer than the water tunnel flow) through the three ducts pierced in the hydrofoil body (see Sec. 2.2 and Figure 3, left). The heated water has a temperature T_e kept constant to a target value, about 15 K higher than the freestream temperature T_∞, thus resulting in a temperature difference between the flow and the model surface of $T - T_\infty = \Delta T \lessapprox 4\ K$. The Richardson non-dimensional number, representing the importance of natural convection relative to forced convection, is $Ri = g(T - T_\infty)C/U_\infty^2 < 0.1$, being g the gravitational acceleration. It is generally assumed that natural convection is negligible for Ri below the critical value $Ri_C = 0.1$, and consequently natural convection in the present tests can be reasonably deemed negligible for all examined test conditions. Moreover, the action of the surface heat flux at the examined test conditions has a negligible effect also on laminar-turbulent transition and flow separation, as reported in Costantini et al. (2015) in a gaseous nitrogen flow and in Miozzi et al. (2019) for the present experimental setup but with the isolated hydrofoil model.

2.5. Test conditions

The experiments were conducted at a single, moderate propeller load (propeller advance ratio $J = 0.88$, freestream speed $U_\infty = 3.4\ m/s$, propeller rotational speed $n = 17\ rps$) for three hydrofoil angles of attack ($AoA = [0^\circ,\ 4^\circ,\ 8^\circ]$). At $AoA = 0^\circ$, the symmetry of the *NACA 0015* hydrofoil leads to a nominal symmetry of the pressure distribution over the two hydrofoil surfaces, thus allowing to limit the study to a single surface; in contrast, at $AoA \neq 0^\circ$ both hydrofoil surfaces require investigation, since the altered pressure distribution leads to the establishment of a "suction" and of a "pressure" hydrofoil side. Therefore, $AoA = 4^\circ$ and 8° require two separate data acquisitions, carried out by maintaining the adjustment of cameras and LEDs fixed while rotating the hydrofoil.

The data acquisition at each experimental condition concerns sequences of images for a duration of about 160 propeller turns, which are sufficient to guarantee the convergence of in-phase statistics (see Sec. 3.3). In the following data presentations, the lengths are dimensionless with the radius of the propeller ($R = 113.5\ mm$), according to the practice adopted in the literature on the subject. It is worth noticing that the Reynolds number with respect to the velocity of the blade tip ($U_{tip} = n\ \pi\ D \approx 12.123\ m/s$) is $Re_{tip} = U_{tip}\ R/\nu = 1.38 \times 10^6$, while its chord counterpart is $Re_{chord} = U_\infty\ C/\nu = 0.408 \times 10^6$.

3. Data preprocessing

3.1. Temperature data extraction

The TSP intensity data acquired by the fast cameras are initially processed as described in Fey et al. (2003), Liu and Sullivan (2005) and Tropea et al. (2007). This common practice has been adopted by this research group in all previous works involving TSP in underwater applications since Capone et al. (2015). It provides the estimation of the instantaneous temperature maps after the elaboration of the intensity images, captured by each camera, according to the following procedure:

- A dark image is extracted by averaging a set of 100 images acquired with *LED* lights off and inactive model heating, where both the water tunnel and the propeller are at rest. The dark image captures the background residual luminosity from the surrounding environment and the thermal noise of the camera;
- A reference image (named as "Ref") is extracted by averaging a set of 100 images acquired with *LED* lights on, inactive model heating, and again both water tunnel and propeller at rest. The acquisition takes place after the model has reached the thermal equilibrium with the water in the tunnel at T_∞, measured during each calibration procedure. The Ref image retains all *LED* lights residual reflections, non-uniform luminophore concentration distribution, and spatial non-uniformity of the *LED* illumination;
- The required number of run images ($\approx 15,000$, ≈ 165 propeller turns) are acquired at the tunnel, propeller and hydrofoil operative conditions, with *LED* lights on and model heating activated. This series of TSP images is named as "Run" dataset.

The dark image is subtracted from the Ref image and Run dataset, with the aim to minimize the presence of background residual light disturbances and the thermal noise from the camera. Then, each Run image is ratioed by the Ref image, to compensate for non-uniform illumination, uneven coating, and non-homogeneous luminophore concentration in the TSP active layer (see Liu and Sullivan (2005) and Tropea et al. (2007)).

The fluid dynamic loads exerted by the flow induce deformations on the model that produce a change in the relative position between the model and the cameras, thus leading to a misalignment between the Ref and Run images. Nevertheless, the careful recovering of the model deformation on each Run image with respect to its reference position minimizes this misalignment (Miozzi et al., 2019). Cross-shaped targets, painted on the model surface at known $3D$ coordinates, are tracked from each Run image against the Ref image. Their differential displacement allows estimating the coefficients of a linear, affine transformation, used to align the images (registration).

Once registered, Run and Ref images are ratioed. The image resulting from this division is projected into the metric $3D$ Euclidean space by following an inverse linear perspective transform, determined by solving the homography that defines the mapping between the targets on the Ref image and their $3D$ position on the model surface. The obtained orthorectified, not uniformly spaced map represents the intensity ratio distribution on the model surface in the reference space $O'\{X_s, Y, Z\}$ (see Figure 3 left). A cubic interpolation extracts the final intensity maps on an equispaced grid of 140 μm cell size, eventually converted to thermal maps using an appropriate calibration curve (Capone et al., 2015). In what follows, X, Y, Z symbols state for distances made non-dimensional by the chord length C.

3.2. Temperature data filtering

The presence of significant noise levels in images capturing fluorescent phenomena is a well-known problem in the scientific community. The nature of the disturbances is assumed to be Additive, White, and Gaussian (AWGN). Benzi et al. (1981) has shown that this type of noise can play a constructive role in detecting weak signals due to Stochastic Resonance (SR), overturning the conventional opinion that considers noise as always as a nuisance (Dodda et al., 2020).

The filtering procedure for the temperature data follows Miozzi et al. (2019). The first step concerns the application of a deformed Gaussian spatial filtering. The proposed filter is an enhanced version of the classical Gaussian blur (Koenderink, 1984). It acts by applying a weak stretch of the kernel normal to the image gradient where the data exhibit a spatially coherent gradient, thus preserving the image edges from smoothing

A second filtering step manages the smoothness of the time series of the temperature in each image pixel by applying a Savitzky-Golay filter with a polynomial order of 1 and a time window of $2T_M + 1 = 11$, where T_M is the impulse-response half-length. This corresponds to a nominal normalized cutoff frequency $f_{nc} = 0.2$ (Schafer, 2011), where the transfer function is 3 dB. The dimensional cutoff frequency of the filtered dataset is $f_c = 0.5 \times 0.2 \times 1500 = 150$ Hz. Figure 5 reports the filtering effect in $T(\mathbf{x}, t) - \overline{T}(\mathbf{x})$ maps, where the application of the filter steps transforms the signal from the original, $AWGN$-affected map on the left in the most decipherable map on the right, revealing the existence of temperature coherent blobs whose details were almost invisible in the original map. As reported hereafter, they represent the detailed fingerprint of a laminar separation bubble, where a warmer separation region is followed by a colder one, cooled by the reattaching flow. The interested reader can find further details about both spatial and temporal filtering steps in Miozzi et al. (2019).

3.3. Decomposition of turbulent quantities in presence of a periodic contribution

A propeller imposes, during its rotation, a neat periodical character to the surrounding flowfield, which propagates to the whole velocity field in its wake. In such a scenario, the

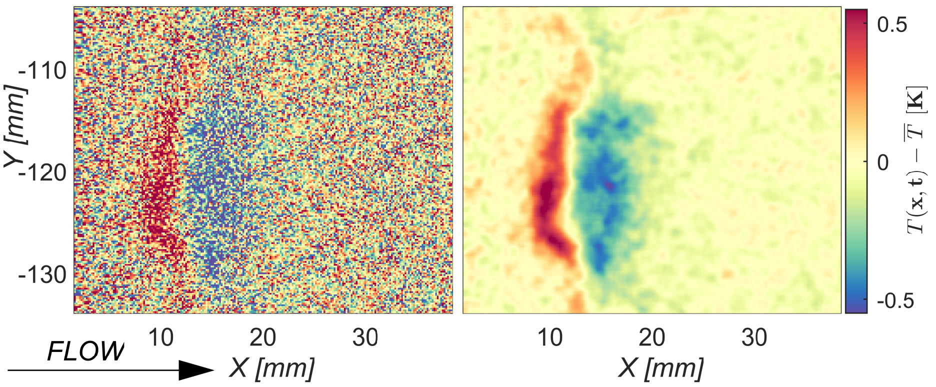

Figure 5: Detail of a region encasing sharp details and flat areas simultaneously: original map of $T(\mathbf{x},\ t) - \overline{T}(\mathbf{x})$ (left) versus its filtered version (right). The two paired, vertically elongated blobs on the left half of the map mark the warmer and colder locations of flow separation and reattachment due to the pressure gradients induced by the hydrofoil incidence ($P_A^{\downarrow}$) and the propeller rotation ($P_P^{\downarrow}$). Flow is from the left.

triple decomposition proposed by Reynolds and Hussain (1972) emphasizes the presence of events having a wave-like periodicity by introducing the phase-average of a turbulent signal as follows:

$$f(\mathbf{x},t) = \bar{f}(\mathbf{x}) + \tilde{f}(\mathbf{x},t_s) + f'(\mathbf{x},t) = \bar{f}(\mathbf{x}) + \tilde{f}(\mathbf{x},\varphi_s) + f'(\mathbf{x},t), \tag{1}$$

where $\bar{f}(\mathbf{x})$ is again the time-average, $\tilde{f}(\mathbf{x},t_s) = \tilde{f}(\mathbf{x},\varphi_s)$ is the statistical contribution of the wave, and $f'(\mathbf{x},t)$ is the random component, while $\mathbf{x}$ is the vector containing the spatial coordinates X, Y and Z, and t is the time. The phase-average is defined over the phase angles $\varphi_s = s\Delta\varphi = \omega t_s \in [0, 2\pi)$ at times $t_s = s\Delta t$, where: s is the set of integers $s \in [0,\ \mathtt{S})$, being $\mathtt{S}$ the number of sampled phase angles; $\Delta\varphi = 2\pi/\mathtt{S}$; and t_s belongs to the interval $t_s = s\Delta t = \in [0, \mathtt{T})$, being $\mathtt{T}$ the characteristic period of the propeller which rotates at angular velocity ω.

The original signal is thus decomposed in a time-average plus two fluctuating terms, one having periodic character, and the other one featuring random behavior. The triple decomposition applied to the set of temperature maps gives:

$$T(\mathbf{x},t) = \overline{T}(\mathbf{x}) + \widetilde{T}(\mathbf{x},\varphi) + T'(\mathbf{x},t), \tag{2}$$

where

$$\overline{T}(\mathbf{x}) = \langle T \rangle_{\mathsf{T}} = \lim_{\mathsf{T}\to\infty} \frac{1}{\mathsf{T}} \int_0^{\mathsf{T}} T(\mathbf{x},t)dt, \quad \widetilde{T}(\mathbf{x},\varphi) = \langle T \rangle_{\mathsf{P}} = \lim_{M\to\infty} \frac{1}{M} \sum_{n=0}^{M} T(\mathbf{x},\varphi_s + 2\pi n) \tag{3a,b}$$

$$\widetilde{T}(\mathbf{x},\varphi_s) = \langle T \rangle_{\mathsf{P}}(\mathbf{x},\varphi_s) - \overline{T}, \quad s \in [0, 2\pi). \tag{4}$$

Following Eq. 4, here we define also the phase-average of the temperature fluctuating part T' as:

$$\widetilde{T}'(\mathbf{x},\varphi_s) = \langle T' \rangle_{\mathsf{P}}. \tag{5}$$

In the same way, the time-averaged standard deviation is defined as:

$$\sigma_T(\mathbf{x}) = \sqrt{\lim_{\mathsf{T}\to\infty} \frac{1}{\mathsf{T}} \sum_{t=0}^{\mathsf{T}} \left[T(\mathbf{x}, t) - \overline{T}\right]^2} \tag{6}$$

4. A double route to move from temperature to skin friction maps

The relationship proposed in this paper, linking temperature and skin friction in a turbulent boundary layer, follows a twofold path. The former considers the fluctuating temperature as a passive tracer. The knowledge of its displacement provides a quantitative estimation of the skin friction field via its relationship with the friction velocity. The latter grounds on the asymptotic expansion of the energy equation at the wall. The obtained optical-flow-like equation relates temperature (scalar) and qualitative skin friction (vector) fields through an ill-posed problem. When dealing with TSP, an inhomogeneity in the heat flux distribution provided by the heating system may induce a biased temperature measurement which affects the instantaneous and averaged temperature values T and $\overline{T}$ but not $\widetilde{T}$ and $\widetilde{T}'$, thus constraining the choice between one or the other approach. This section illustrates two techniques grounding on the passive tracer assumption (Sec. 4.1) and the other one based on the optical-flow analogy (Sec. 4.2), ending with a short discussion about the strategies adopted to maximize the information despite the temperature bias (Sec. 4.3).

4.1. A link between celerity of propagation of thermal disturbances and friction velocity

The properties featured by the displacement of passive scalars in a turbulent boundary layer, when observed at decreasing distance from the wall, provide a counterintuitive representation of the complexity of the dynamics inside the TBL. Far from the wall, at non-dimensional wall-normal distance $Z^+ > 7$ (where $Z^+ = Zu_\tau/\nu_\infty$, being u_τ the absolute value of the friction velocity and ν_∞ the kinematic viscosity of the freestream), a passive scalar embedded in a moving fluid displaces at the velocity of the surrounding environment. However, this behavior is observed only above a certain distance from the wall. In his pioneering work, Eckelmann (1974) reported the divergence between the local flow velocity and the celerity of propagation of velocity disturbances when the measurement location approaches the wall. Close to the wall, in the range $0 < Z^+ < 7$, the following statements hold:

$$\lim_{Z^+\to 0} \bar{\mathbf{u}} \quad = 0 \tag{7}$$

$$\lim_{Z^+\to 0} \overline{\mathbf{U}}_p = c\mathbf{u}_\tau \tag{8}$$

where $\bar{\mathbf{u}}$ and $\mathbf{u}_\tau$ are themean and the friction velocity vectors respectively, and $\mathbf{U}_p$ is the propagation celerity of velocity disturbances. While the time-averaged flow velocity goes to zero, the velocity disturbances propagate faster than the surrounding flow; in practice, they behave as a wave, which propagates at a celerity proportional to the

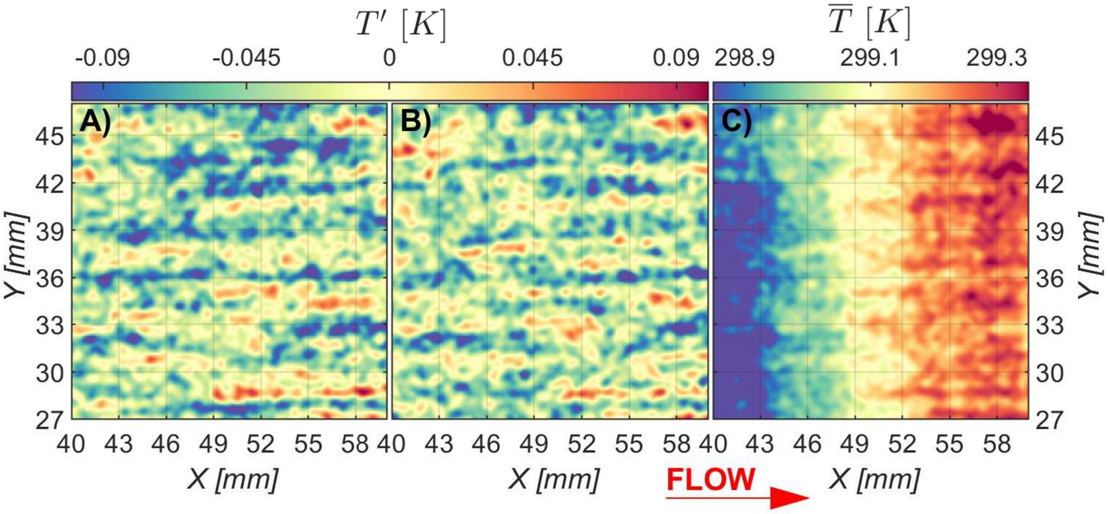

Figure 6: Details of couple of T' (snapshots A, B) acquired at time $t_{1,2} = t_0 \pm 3\ ms$ and $\overline{T}$ (snapshot C) acquired at time $t_0 = 53\ ms$ for the hydrofoil in crossflow configuration at $AoA = 10°$. The couple of images in A) and B) feed the thermal-blobs-tracking TR algorithm, while the single map in A) feeds the energy-equation-based OF algorithm. Larger sequence of T' also feeds TH algorithm. Both datasets share the same spatial extension and are acquired close to the same instant t_0. Wide differences appearing in thermal range dominion testify the lack of correlation between the approaches.

friction velocity $\mathbf{u}_\tau$ by a constant factor c. The term "celerity" is indeed adopted here to resemble the similarity to a wave.

Subsequent findings in literature (see Kim and Hussain (1993), Johansson et al. (1991) and Geng et al. (2015) among others) are all in good agreement, providing that in the viscous sublayer ($Z^+ < 5$) of a turbulent channel, the streamwise propagation celerity of disturbances of velocity and vorticity are constant, and their $3D$ components range between $[9\,u_\tau - 10\,u_\tau]$ and $[8\,u_\tau - 10\,u_\tau]$. respectively (Geng et al. (2015)). Hetsroni et al. (2004) established a relationship also between the celerity of propagation of temperature disturbances $\mathbf{U}_{pT}$ and $\mathbf{U}_p$, which depends on the thermal boundary condition at the wall and on the Prandtl number Pr:

$$\mathbf{U}_{pT}^{+} = Pr^{-1/2}\mathbf{U}_{p}^{+} \tag{9}$$

for constant wall heat flux, and

$$\mathbf{U}_{pT}^{+} = Pr^{-1/3}\mathbf{U}_{p}^{+} \tag{10}$$

for constant wall temperature. The measurement of $\mathbf{U}_{pT}$ would thus provide a shortcut for the measurement of $\mathbf{u}_\tau$ and of the friction-related quantities.

4.1.1. Minimizing dissimilarity from Taylor Hypothesis: the TH algorithm In their seminal paper, Del Álamo and Jiménez (2009) proposed a physically motivated definition of the convection velocity of a passive scalar, for the case in which it depends on the spectral information in only one direction, either space or time, and on a local derivative in the remaining direction. The minimization of the dissimilarity between the ideal wave behavior (conform to the Taylor hypothesis) and the observed one allows to estimate the reference frame (in fact, its absolute value) in which waves experience the least amount of change.

Miozzi et al. (2020b) extended the aforementioned method to the study of the non-homogeneous flow on the suction side of a hydrofoil model at incidence. Under the assumption that the temperature fluctuations at the wall behave like a passive scalar, the streamwise propagation celerity component $U_{X,pT}$ was obtained by minimizing the discrepancy of the energy transport equation from the Taylor hypothesis (Geng et al., 2015). The method presented in Miozzi et al. (2020b) is here further extended to the spanwise propagation celerity component $U_{Y,pT}$; the analysis focuses on the evolution of $\widetilde{T}(\mathbf{x},\varphi_s)$, which captures the phase-dependent main features of the surface temperature due to the wake flow, and to $T'(\mathbf{x},t)$, which describes the randomly fluctuating contribution (see Sec. 3.3). It is worth to notice that while both $\widetilde{T}$ and T' have a null mean, the time-averaged skin friction corresponding to their underlying structures has not. The application of the TH algorithm to the set of $\widetilde{T}$ estimates the non-zero ensemble-averaged friction velocity contribution $\langle \boldsymbol{u}_\tau(\widetilde{T})\rangle_\varphi$, as reported in the following. Spatial and temporal gradients are evaluated with central differences on a spatial lag of 4 px, similarly to what reported in Miozzi et al. (2020b), using the procedures proposed in Hosseini and Plataniotis (2017). The friction velocity components u_τ and v_τ are then computed as $u_{\tau X} = U_{X,pT}/c$ and $u_{\tau Y} = U_{Y,pT}/c$, where $c = 5.54$ is the constant of proportionality at constant wall temperature for the present case, see Miozzi et al. (2019).

4.1.2. Tracking of thermal blobs: the TR algorithm Figures 6 A)B) report the detail of two snapshots of T', acquired at a temporal distance of 7 ms for the isolated hydrofoil in crossflow configuration at $AoA = 10°$. Streamwise-elongated structures characterize the texture of the thermal field. Their origin can be associated with the wash-up/wash-down action of vortical structures impinging on the hydrofoil surface. Comparison between snapshots A) and B) allows identifying a neat displacement of such structures, which suggests adopting an approach in analogy with Particle Image Velocimetry (PIV). However, the application of a tracking tool to the present research is subject to several requirements, which are not exactly covered by the standards of classical PIV-algorithms. The deformable nature of the thermal traces moving on the hydrofoil surface imposes robustness as a leading requirement of the procedure. Moreover, the large dimension of the involved temperature dataset ($\approx$ 15000 maps 1982×742 px in size, 85.5 GB of disk space) puts the efficiency of the tracking as a further mandatory requirement. Among the well represented class of optical-flow algorithms, recently Kroeger et al. (2016) proposed a new approach, based on Dense Inverse Distance (DIS), to extract robustly estimated dense flow between couples of images at unprecedented speed. The algorithm, named DIS optical flow, relies on three successive steps:

- Fast inverse search for sparse correspondences;
- Densification to compute a dense flow field $\boldsymbol{U}_s$;
- Variational refinement of $\boldsymbol{U}_s$.

The fast search of correspondences relies on the optimized inverse approach to the classical Lukas-Kanade procedure (Lucas and Kanade, 1981) proposed by Baker and Matthews (2004). The method presented above, and here named *TR* algorithm, is applied in this work for the first time to determine $\mathbf{U}_{pT}$ components and thus the friction velocity $\boldsymbol{u}_\tau$ (see Sec. 4.1.1). As a suggestion about its capability, Sec. 5.5 reports the map of $|u_{\tau Y}|$, showing the footprint of the hub vortex $\mathbb{H}$ obtained via the TR algorithm.

4.2. Solving the energy equation at the wall: the OF algorithm

Liu and Woodiga (2011) proposed to relate the temperature map to the skin-friction vector field by rearranging the asymptotic form of the energy equation at the wall in a form structurally equivalent to the Optical Flow *OF* equation (Horn and Schunck (1981)). The minimization of an appropriate functional that contains the Horn-Schunk regularization term provides an Euler-Lagrange equation, which can be solved as an inverse problem following the variational approach. All the higher order unknown terms can be lumped into a forcing component, whose initial magnitude is estimated by adopting a simple heat-flux model and then iteratively refined. An extension of the same scheme to time- and phase-averaged quantities is given in Miozzi et al. (2016).

By using the Taylor expansions of the velocity and temperature fields near a wall in a flow, the asymptotic form of the energy equation at the wall can be written as

$$G + \tau_i \frac{\partial T_w}{\partial X_i} = 0 \tag{11}$$

where $\tau_i = \mu(\dfrac{\partial u_i}{\partial Z})_w$ are the skin-friction components, and G is a term containing the time rate of the heat flux, the thermal diffusion and the viscous dissipation contributions (Liu and Woodiga (2011)). Eq. 11 gives a relation between skin-friction vector, heat flux and temperature at the wall. It represents a balance between the skin-friction vector projected on the normal vector ∇T_w to an isotemperature line $T_w = const$ and the term G. Alternatively, $\tau_i \frac{\partial T_w}{\partial X_i}$ can be formally interpreted as the flux of a scalar T_w transported by a skin-friction field τ_i, while G is considered as a source term. In a sense, it is a differential form of the Reynolds analogy Liu and Woodiga (2011).

By introducing the triple decomposition of Eq. 1 into Eq. 11, and following Miozzi et al. (2016), the equations for the time- and phase-averaged quantities are obtained as:

$$G_0 + \frac{\langle \tau_i \rangle_\mathsf{T}}{\tau_{ref}} \frac{\partial \langle T_w \rangle_\mathsf{T}}{\partial X_i} = 0, \tag{12}$$

$$\widehat{G}_0 + \frac{\langle \tau_i \rangle_{\mathsf{P}}}{\tau_{ref}} \frac{\partial \langle T_w \rangle_{\mathsf{P}}}{\partial X_i} = 0, \tag{13}$$

where G_0 and $\widehat{G}_0$ are defined as:

$$G_0 = \frac{\langle \epsilon \rangle_{\mathsf{T}}}{\tau_{ref}} + \frac{1}{\tau_{ref}} \langle \tau_i' \frac{\partial \langle T_w \rangle_{\mathsf{T}}}{\partial X_i} \rangle_{\mathsf{T}}, \tag{14}$$

$$\widehat{G}_0 = \frac{\langle \epsilon \rangle_{\mathsf{P}}}{\tau_{ref}} + \langle \frac{\tau_i'}{\tau_{ref}} \frac{\partial T_w'}{\partial X_i} \rangle_{\mathsf{P}} + \frac{h_p}{k_f} \frac{1}{Re_{ref} u_{\tau_{ref}}} \frac{\partial \langle T_w \rangle_{\mathsf{P}}}{\partial t}. \tag{15}$$

In the above equations, ϵ groups higher order terms, τ_{ref} is a reference value of skin friction, arbitrarily fixed to the maximum of the τ field magnitude, h_p is the thickness of the polymer layer, and k_f is the thermal conductivity of the fluid. Based on τ_{ref}, both $u_{\tau_{ref}}$ and Re_{ref} are derived, according to their definition:

$$u_{\tau_{ref}} = \sqrt{\tau_{ref}/\rho} \tag{16}$$

$$Re_{ref} = u_{\tau_{ref}}\ h_p/\nu. \tag{17}$$

For a full description of the algorithm and its intrinsic limitations, including an uncertainty analysis, the interested reader is referred to Liu and Woodiga (2011) and Miozzi et al. (2016).

4.3. What analysis for which data: maximizing the information from a biased setup

The model configuration reported in Sec. 2.2 is affected by the suboptimal arrangement of the heating system and thus by a biased heat flux. As discussed in Miozzi et al. (2019), obtaining a uniform Biot number $B_i = \frac{h}{k} L_c$ over the whole *NACA* 0015 hydrofoil surface requires a great deal of effort with not fully satisfactory results. In the Biot number definition, k_p is the thermal conductivity of the model body and L_c is the non-uniform distance between the heating system and the heat removing location, i.e. the hydrofoil surface. Although the surface temperature distribution established by the heat-exchanging ducts in the fore and mid-chord region of the (isolated) hydrofoil can be reasonably considered as uniform, the rapid reduction of the hydrofoil thickness downstream of $X \approx 0.65$ and the increasing distance from the aft heat-exchanging duct leads to a temperature decrease towards the trailing edge (see Figure 7), since the heat removed by the action of the surrounding flow cannot be restored by the heating system at the required rate. In the present work, an influence of the non-uniform imposed heat flux is visible also in regions where the flow-induced temperature gradients are small, such as in the model surface region within the propeller streamtube (see Sec. 5.2).

To a first order of approximation and under the hypothesis of small-scale heat flux, it can be assumed that the biased heat flux has an influence only on the mean-temperature term $\overline{T}$, while both fluctuating random and periodic parts of the triple decomposition in Eq. 4, i.e. $T'(\mathbf{x}, t)$ and $\widetilde{T}(\mathbf{x}, \varphi_s)$, are not affected by the non-uniform imposed heat flux. Accordingly, the data analysis involving $\overline{T}$ is reliable only up to $X \approx 0.65$, while no bias affects the analysis of periodic and random fluctuations.

The skin-friction estimation methods previously described rely in a different way on each of the terms of the triple decomposition: the OF algorithm, which works on temperature gradients from single images, can be fed by $T(\mathbf{x},\ t)$, $\overline{T}(\mathbf{x})$ or $\widetilde{T}(\mathbf{x},\varphi_s)$ and returns a relative (normalized) skin-friction vector field $\boldsymbol{\tau}/\tau_{ref}$ for each provided temperature map. On the other hand, the TR algorithm requires pairs of $T'(\mathbf{x},t)$ maps separated by a specific time lag Δt and returns a field of $\boldsymbol{U}_{pT}(\boldsymbol{x},t)$, while the TH algorithm is fed by maps of $\widetilde{T}(\mathbf{x},\varphi_s)$ and $T'(\mathbf{x},t)$ and returns the modulus of the ensemble- or time-averaged components $|U_{X,pT}|$, $|U_{Y,pT}|$. As discussed in Sec. 4.1, the propagation celerity of temperature disturbances $\boldsymbol{U}_{pT}$ is in direct relationship with $\boldsymbol{u}_\tau$, and thus enables the determination of absolute $\boldsymbol{\tau}$-fields.

5. Results

5.1. Synopsis of results

The application of the triple decomposition from Eq. 2 to data collected during the present experiments provides three datasets, whose analysis unveils different and simultaneous phenomena of interaction between the flow and the model surface. As introduced in Sec. 1, these phenomena belong to, at first glance, two main classes: those involving manifolds originating at the propeller level, i.e. the blade tip ($\mathbb{T}$), the propeller hub ($\mathbb{H}$) and the blade wake ($\mathbb{W}$) coherent structures, and those originating at model surface level, i.e. the LSB ($\mathbb{L}$) and the trailing-edge separation ($\mathbb{S}$) ones. For the better understanding of the graphs of the investigated quantities presented in the following sections, some comments are considered important at this point. In each figure, both hydrofoil model surfaces are shown as seen from above, with the hydrofoil suction and pressure surfaces on top and bottom of the figures, respectively. In practice, the hydrofoil surfaces are rotated around the leading edge (located at $X = 0$) and unfolded in the streamwise direction. The suction and pressure conditions due to the $AoA \neq 0°$ are indicated by $P_A^{\downarrow}$ and $P_A^{\uparrow}$ respectively. The flow direction is indicated by a red arrow, and is from the bottom for the top figures (suction surface) and from the top for the bottom figures (pressure surface). Obviously, the subdivision into suction and pressure surfaces at the symmetry condition $AoA = 0°$ ($P_A^{\updownarrow}$) is customary and is done here only for the sake of consistency with the other figures.

The projection of the propeller hub axis on the plane of the unfolded hydrofoil surfaces (see above) is marked as a black-edged red dot. It is located at $X = 0$ and $Y = 0$. The dashed black circumference has a radius coinciding with that of the propeller blades. The black arrows show the spin of the propeller.

The rotation of the propeller streamtube induces over- and under-pressure regions on the hydrofoil surfaces, which are marked as $P_P^{\uparrow}$ and $P_P^{\downarrow}$, respectively. This leads to four different conditions in the figure quadrants:

- $[P_A^{\downarrow} P_P^{\downarrow}]$ in the top right quadrant, where the suction condition due to the hydrofoil incidence is enhanced by the under-pressure induced by the propeller;

- $[P_A^{\downarrow} P_P^{\uparrow}]$ in the top left quadrant, where the suction condition due to the hydrofoil incidence combines with the over-pressure induced by the propeller;
- $[P_A^{\uparrow} P_P^{\downarrow}]$ in the bottom left quadrant, where the pressure condition due to the hydrofoil incidence combines with the under-pressure induced by the propeller;
- $[P_A^{\uparrow} P_P^{\uparrow}]$ in the bottom right quadrant, where the pressure condition due to the hydrofoil incidence is enhanced by the over-pressure induced by the propeller.

Accordingly, the flow experiences different pressure distributions in the streamwise direction in the four quadrants. These lead to the peculiar evolution of surface temperature distributions and skin-friction topologies, as described in the next sections. The exposition of the results follows the progression of the flow manifolds $\mathbb{L}$ and $\mathbb{T}$, representing supplementary streamwise and spanwise boundaries of different domains in the wake-hydrofoil interaction, as well as $\mathbb{W}$, $\mathbb{H}$ and $\mathbb{S}$, constrained within the aforementioned borders.

5.2. Laminar separation bubble and manifold $\mathbb{L}$

The first subject covered in the present discussion is the manifold $\mathbb{L}$, i.e. the laminar separation bubble LSB as it appears when interacting with the incoming wake within and outside the propeller streamtube. It is initially investigated by looking at the surface distribution of time-averaged temperature $\overline{T}$ at $AoA = 8°$ and standard deviation σ_T at $AoA = [0°,\ 4°,\ 8°]$ reported in Figure 8 and 9, as well as by looking at $\overline{T}$ and σ_T profiles extracted inside and outside of the propeller streamtube and presented in Figures from 7 to 11. As described in Sec. 4.3, maps of $\overline{T}$ retain the bias due to the suboptimal heating system, which leads to a spanwise oriented strip of lower temperature close to the trailing

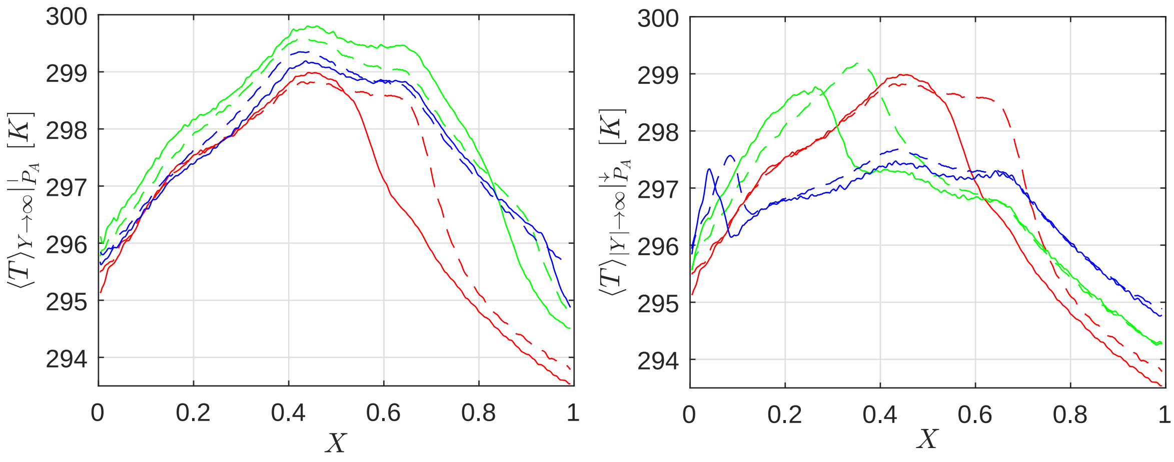

Figure 7: Spanwise averaged $\langle\overline{T}\rangle_{|Y|\to\infty}$ of mean temperature map over a spatial interval out of the propeller streamtube. Pressure $P_A^{\uparrow}$ (left) and suction $P_A^{\downarrow}$ side (right). Red, green and blue colors refer to $AoA = [0°,\ 4°,\ 8°]$, while continuous and dashed styles stand for $[P_P^{\downarrow}]$ and $[P_P^{\uparrow}]$ respectively.

edge (starting at $X \approx 0.65$). Moreover, the thermal signatures of the heat-exchanging ducts become visible as higher temperature strips also in regions where the flow-induced $\overline{T}$-gradients are too small, as compared to those due to the non-uniform imposed heat flux; this occurs e.g. in regions within the propeller streamtube. Figure 8, left reports, as an exemplary case for the effects induced by the flow and by the suboptimal heating system, the $\overline{T}$ map at $AoA = 8°$, and Figure 7 provides a quantitative sketch of the kink-shaped deformations induced by the heating system on temperature profiles out of the propeller streamtube on both $P_A^{\uparrow}$ and $P_A^{\downarrow}$ sides. The same graph provides also a quite accurate representation of the limits of the $\overline{T}$ reliability and suggests its use in regions close to the leading edge, i.e. upstream of $X = 0.65$. On the contrary, the maps of σ_T are not affected by the influence of the non-uniform imposed heat flux, and thus provide notable information about the flow dynamics over the model surface.

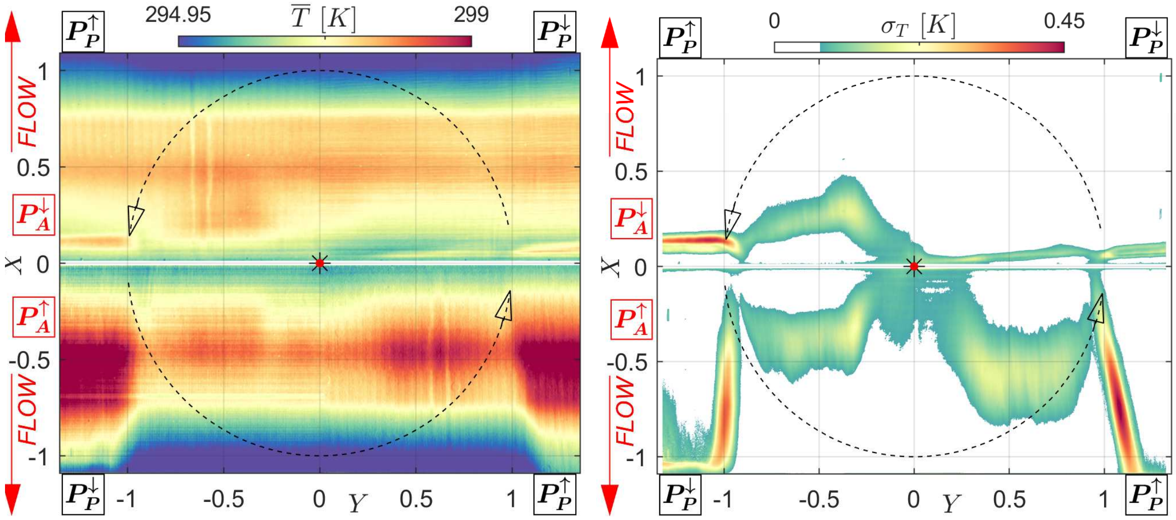

Figure 8: Maps of time average and standard deviation of temperature at $AoA = 8°$: $\langle T \rangle_{\mathsf{T}}$ (left) and σ_T (right). On the hydrofoil suction surface ($P_A^{\downarrow}$), segments of manifold $\mathbb{L}$ displaces towards the leading edge because of the adverse pressure gradient, modulated by positive and negative P_P and deformed by the incoming manifold $\mathbb{W}$. On the hydrofoil pressure surface ($P_A^{\uparrow}$), the adverse pressure gradient loses intensity and separation, if any, occurs closer to the trailing edge.

The first features emerging from the analysis of the temperature results at all AoAs are spanwise-oriented strips with high σ_T (Figure 8, right, and 9), observed on both $P_A^{\downarrow}$ and $P_A^{\uparrow}$ surfaces (the latter except for $AoA = 8°$) in the region outside of the propeller streamtube, corresponding to narrow strips at higher $\overline{T}$ observable in Figure 8, left, close to the leading edge. These relative maxima are also observable in the profiles shown in Figures 7 and 10 (right). These graphs report the streamwise distributions of $\overline{T}$ and σ_T, obtained as spanwise averages of the respective maps in the regions outside of the propeller streamtube and indicated as $|Y| \to \infty$, for both the pressure and the suction sides of the hydrofoil. Here solid and dashed lines refer to the $P_P^{\downarrow}$ and

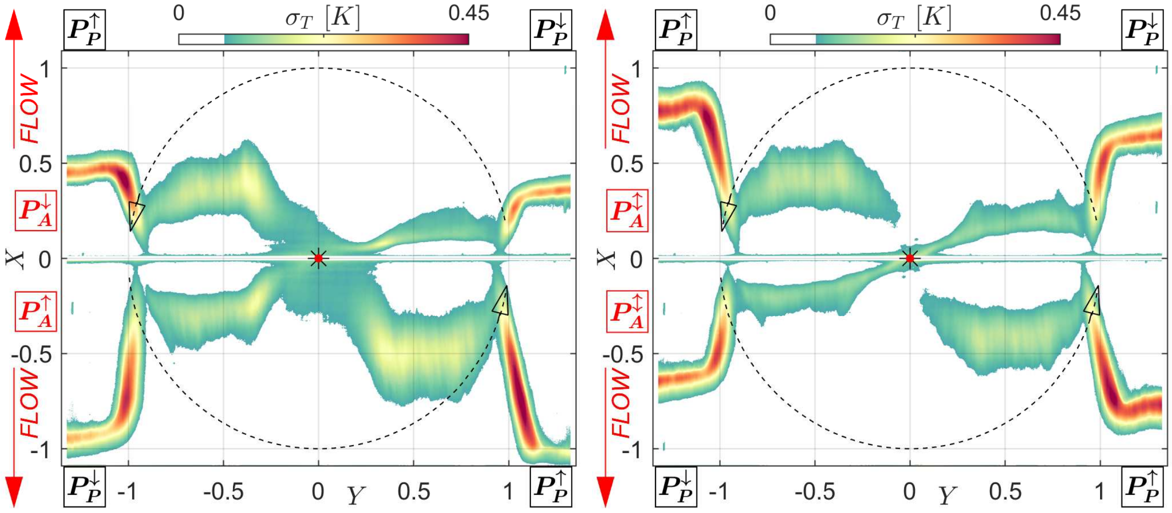

Figure 9: Maps of standard deviation of temperature σ_T at $AoA = 4°$ (left) and $AoA = 0°$ (right), as described for Figure 8 (right). On $P_A^\uparrow$ side, reducing AoA displaces separation towards the leading edge. Separation and transition out of the streamtube occurs within the hydrofoil length.

$P_P^\uparrow$ quadrants, respectively. It is worth to notice that profiles of $\overline{T}$ in Figure 7 can capture such events only for the suction side at $AoA = [4°, 8°]$ because, in all other conditions, they are located too close to the trailing edge and smeared by the heating system. Miozzi et al. (2019) report that similar flow features, for the same hydrofoil model in crossflow, are induced by the flow evolution within a laminar separation bubble. The less efficient heat removal via the action of the flow within the LSB leads to a local maximum of $\overline{T}$ in the vicinity of the separation location, while the reattachment location is close to the end of the negative $\partial\overline{T}/\partial X$ region following the local $\overline{T}$-maximum. Downstream of separation, the disturbances in the still laminar boundary layer undergo strong amplification, which induces transition to turbulence and eventually turbulent flow reattachment. Although the laminar-turbulent transition process occurs over a certain distance, a "transition location" can be identified at a physically significant location in the transition region. As discussed in Costantini (2016) and Miozzi et al. (2019), the location of the maximal gradient of $\partial\overline{T}/\partial X$ within the transitional region is an appropriate transition location; this position is in agreement with the location corresponding to $\sigma_{T,max}$ (Miozzi et al., 2019), in a manner similar to the association between the transition location and the peak in the standard deviation of the pressure coefficient σ_{c_p} presented in Gardner and Richter (2015). Outside of the propeller streamtube, the boundary-layer evolution in the streamwise direction can be assumed (at least in a first approximation) to be analogous to that observed on the isolated hydrofoil. Accordingly, the aforementioned regions on the hydrofoil suction surface following the maxima of $\overline{T}$ are expected to be laminar separation bubbles, in analogy with Miozzi et al. (2019). Similarly, the maximum in σ_T, which

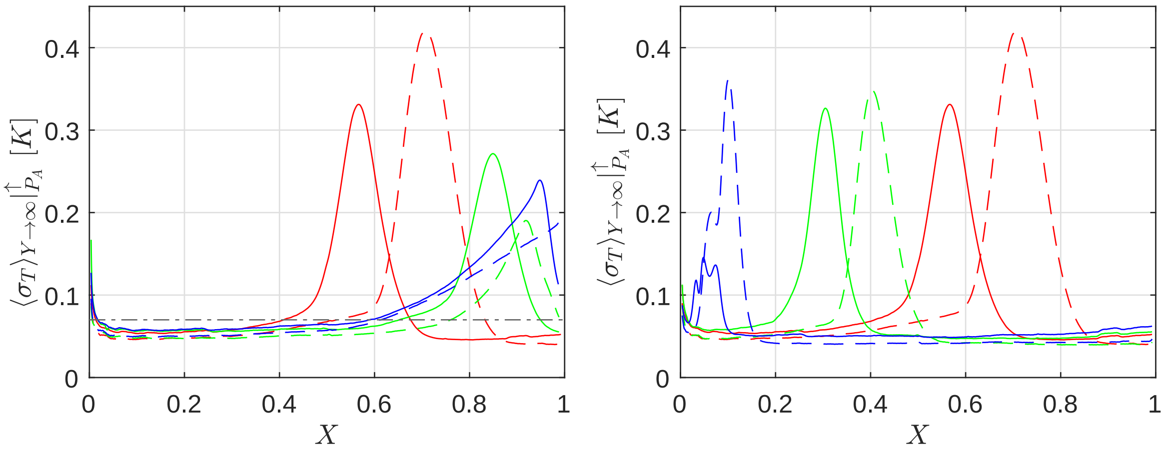

Figure 10: Spanwise averaged $\langle\sigma_T\rangle_{|Y|\to\infty}$ of the map of temperature standard deviation over a spatial interval out of the propeller streamtube. Pressure $P_A^{\uparrow}$ (left) and suction $P_A^{\downarrow}$ side (right). Red, green and blue colors refer to $AoA = [0°,\ 4°,\ 8°]$, while continuous and dashed styles stand for $[P_P^{\downarrow}]$ and $[P_P^{\uparrow}]$ respectively.

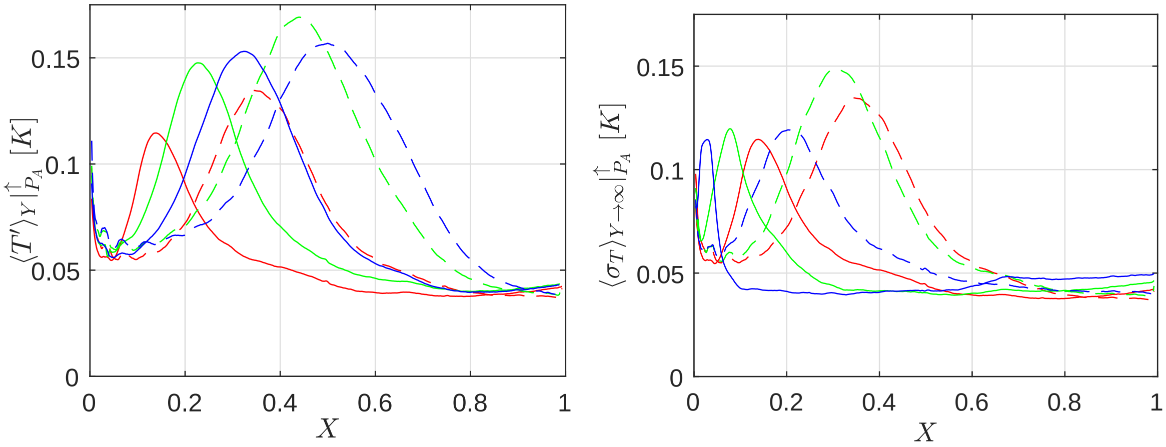

Figure 11: Spanwise-averaged $\langle\sigma_T\rangle_{|Y|\in PS}$ of the map of temperature standard deviation over a spatial interval inside the propeller streamtube. Pressure $P_A^{\uparrow}$ (left) and suction $P_A^{\downarrow}$ side (right). Red, green and blue colors refer to $AoA = [0°,\ 4°,\ 8°]$, while continuous and dashed styles stand for $[P_P^{\downarrow}]$ and $[P_P^{\uparrow}]$ respectively.

is in agreement with the location of $|\partial\overline{T}/\partial X|_{max}$, is expected to correspond to the location of transition within the LSB. These expectations are confirmed by the skin-friction topologies presented in Figures 12 and 13, which are obtained via OF algorithm applied to the time-averaged surface temperature distributions on the hydrofoil suction surface (see Sec. 4.2). The details reported in these figures show the time-averaged $\mathbb{L}$ manifold at $AoA = 8°$. As discussed e.g. in Liu (2013), Miozzi et al. (2016) and Miozzi et al. (2019), the skin-friction lines determined by means of the OF algorithm provide a physics-based criterion for the identification of separation and reattachment lines (critical lines). In fact, convergence and divergence of skin-friction lines identify spatial *loci* of separation and reattachment (Lighthill, 1963; Hirschel et al., 2014). The topology of $\langle \boldsymbol{\tau} \rangle_{\mathsf{T}}$ in the quadrant $[P_A^{\downarrow} P_P^{\downarrow}]$ (Figure 13) shows a LSB developing for the whole considered span width ($Y \in [0, 1.2]$). In the region outside of the propeller streamtube, the flow separates at $X \approx 0.05$ and reattaches at $X \approx 0.10$. Similarly, the topology of $\langle \boldsymbol{\tau} \rangle_{\mathsf{T}}$ in the quadrant $[P_A^{\downarrow} P_P^{\uparrow}]$ (Figure 12) shows a LSB developing in the region outside of the streamtube, at approximately $Y < -1$. Here, the flow separates at $X \approx 0.1$ and reattaches at $X \approx 0.16$, i.e. the LSB is shifted downstream of the corresponding location in the $[P_A^{\downarrow} P_P^{\downarrow}]$ quadrant because of the influence of the propeller under-pressure. The application of the TH algorithm (see Sec. 4.1.1) provides a further confirmation of the separation and reattachment locations. Figures 14, 15 and 16 present, on the left side, maps of the modulus of the time-averaged friction velocity $\langle |\mathbf{u}_{\tau}| \rangle_{\mathsf{T}}$ while on the right side they report maps of the ensemble-averaged modulus of the phase-averaged streamwise component of the friction velocity $\langle |\tilde{u}_{\tau X}| \rangle_{\varphi}$. This time, outside of the propeller streamtube, the LSB appears as two spanwise-oriented strips with $\langle |\mathbf{u}_{\tau}| \rangle_{\mathsf{T}} \to 0$, separated by a narrow strip with larger $|\langle \tilde{\mathbf{u}}_{\tau} \rangle_{\mathsf{T}}|$. The two former strips correspond to the separation and reattachment lines, whereas the latter strip corresponds to the region of negative skin friction within the LSB.

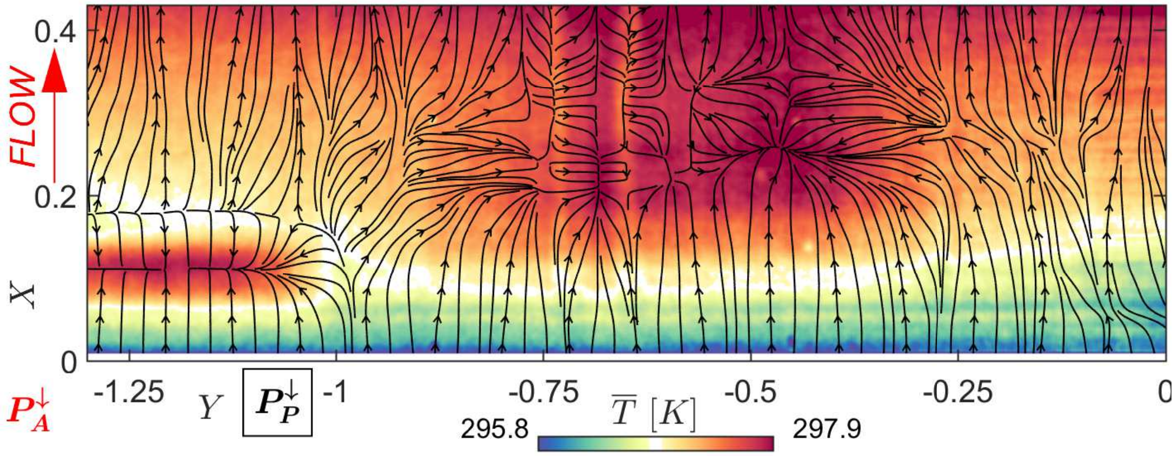

Figure 12: Topology of skin-friction vector field $\boldsymbol{\tau}_w$ overlapped to $\langle T \rangle_{\mathsf{T}}$ on the hydrofoil suction side ($P_A^{\downarrow}$) with propeller-induced over-pressure ($P_P^{\uparrow}$). Convergent and divergent skin-friction lines out of the propeller streamtube ($Y < -1$) mark narrow warmer and colder strips, originating at separation and reattachment *loci* of the still active LSB. Inside the streamtube, the combination of $P_A^{\downarrow}$ and $P_P^{\uparrow}$ displaces a hazy blade signature towards the trailing edge.

On the hydrofoil pressure surface, the boundary layer outside of the propeller streamtube undergoes acceleration over most of the hydrofoil chord length. For this reason, separation occurs further downstream than on the suction side. The occurrence of flow separation close to the hydrofoil trailing edge in the quadrant $[P_A^{\uparrow} P_P^{\downarrow}]$ is confirmed

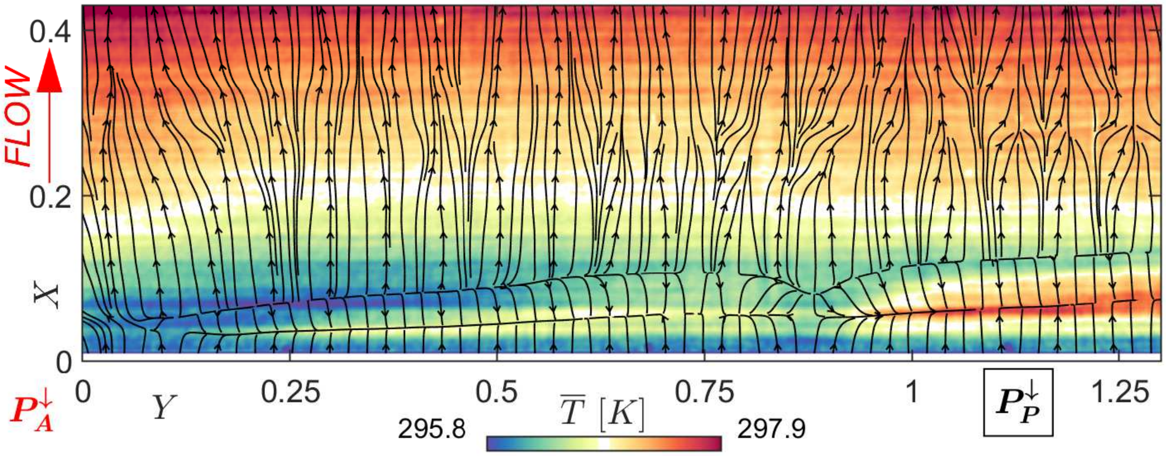

Figure 13: Topology of skin-friction vector field $\boldsymbol{\tau}_w$ overlapped to $\langle T\rangle_{\mathsf{T}}$ on the hydrofoil suction side ($P_A^{\downarrow}$) with propeller-induced under-pressure ($P_P^{\downarrow}$). Convergent and divergent skin-friction lines in and out of the propeller streamtube ($Y > 0.85$) mark narrow warmer and colder strips, originating at separation and reattachment *loci* of the still active LSB. The combination of $P_A^{\downarrow}$ and $P_P^{\downarrow}$ enhances the pressure minimum and the following adverse pressure gradient, thus displacing the LSB towards the leading edge.

by the spanwise-oriented strip with $\langle|\mathbf{u}_\tau|\rangle_{\mathsf{T}} \to 0$ in Figure 16.

The presented comprehensive dataset of surface temperature and skin-friction allows

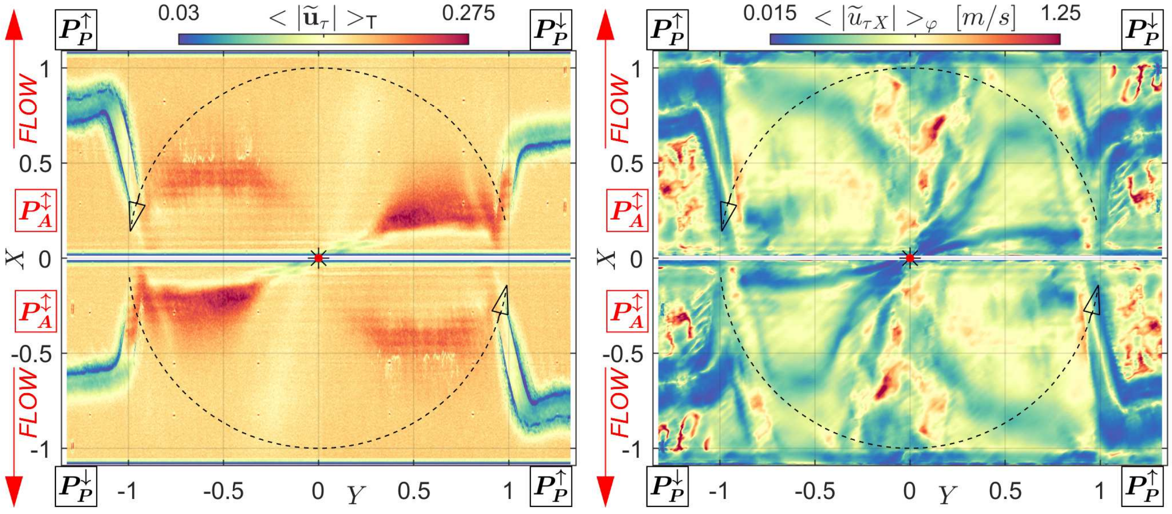

Figure 14: Modulus of time $\langle|\boldsymbol{u}_\tau|\rangle_{\mathsf{T}}$ (left) and ensemble average of phase-averaged friction velocity streamwise component $\langle|\widetilde{u}_{\tau X}|\rangle_{\varphi}$ (right) evaluated with TH algorithm at $AoA = 0°$. Black arrows on right side mark the signature of the tip vortex ($\mathbb{T}$) passage.

studying the spatial evolution of the LSB in the four quadrants and at different AoA. In particular, *loci* of high σ_T appear as reasonable identifiers for the position of the manifold

$\mathbb{L}$, and this information is substantiated by the maps of $|\langle \tilde{\mathbf{u}}_\tau \rangle_\mathsf{T}|$. Outside of the propeller streamtube, the hydrofoil boundary layer still seems to be influenced by the propeller-induced under- and over-pressure, which enhances or weakens the pressure minimum and the following adverse pressure gradient. In fact, on the same hydrofoil surface (suction or pressure), the propeller-induced pressure distribution leads to a displacement of the LSB, which can be summarized as follows: when the propeller induces over-pressure ($P_P^\uparrow$), the effective AoA appears as decreased, and the LSB is displaced into a more downstream location, as compared to the region with propeller-induced under-pressure ($P_P^\downarrow$), where the effective AoA appears as increased. This evolution can be seen also

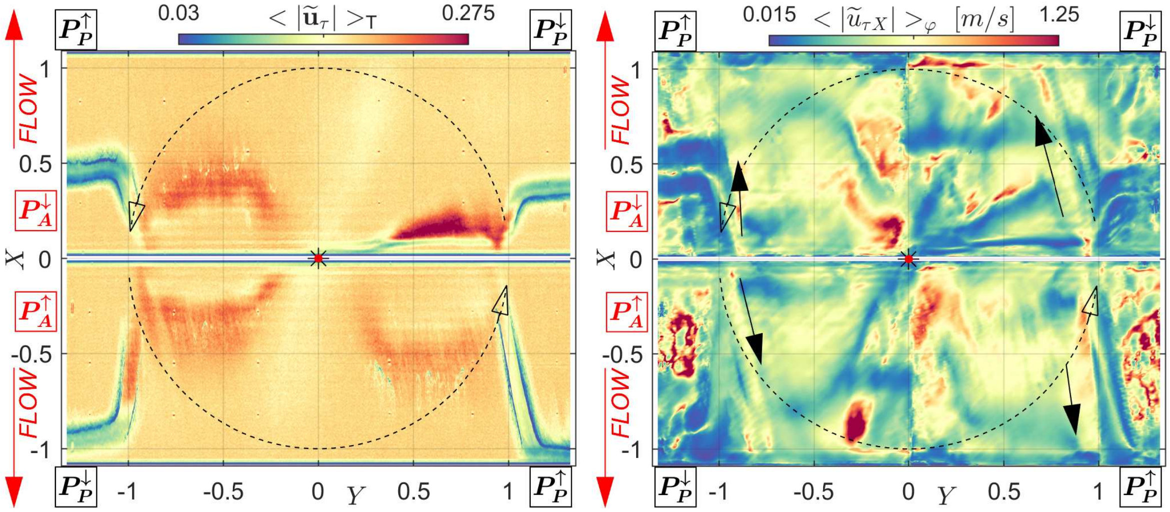

Figure 15: Modulus of time $\langle |\boldsymbol{u}_\tau| \rangle_\mathsf{T}$ (left) and ensemble average of phase-averaged friction velocity streamwise component $\langle |\widetilde{u}_{\tau X}| \rangle_\varphi$ (right) evaluated with TH algorithm at $AoA = 4°$. Black arrows on right side mark the signature of the tip vortex ($\mathbb{T}$) passage.

by comparing the locations of the $\sigma_{T,max}$ and $|\langle \tilde{\mathbf{u}}_\tau \rangle_\mathsf{T}| \to 0$ strips on the same hydrofoil surface but for different AoA in Figures 8 (right), 9 and 14 to 16.

While $\mathbb{L}$ preserves the manifold orientation outside of the propeller streamtube (i.e. $\mathbb{L}$ remains oriented essentially spanwise), inside the streamtube ($|Y| \in PS$) the radial distribution of the propeller-induced pressure field in general causes a strong deformation of the $\mathbb{L}$-structure. This effect can be seen as deformed $\sigma_{T,max}$-regions in Figures 8 (right) and 9. It appears to be related to the interaction between $\mathbb{L}$ and the manifold $\mathbb{W}$, which originates from the trailing edge of the propeller blades. A deformation of the LSB due to the additional forcing produced by the incoming blade wake, suggested by the deformed σ_T-signature, is confirmed for the quadrant $[P_A^\downarrow P_P^\uparrow]$ at $AoA = 8°$ by the skin-friction topological map in Figure 12. In this case, the combination of opposing effects due to $P_A^\downarrow$ and $P_P^\uparrow$ leads to the displacement of a hazy blade signature towards the trailing edge. In contrast, the constructive coupling of $P_A^\downarrow$ and $P_P^\downarrow$ in the other quadrant on the hydrofoil suction surface guarantees the maintaining of a nearly-two-

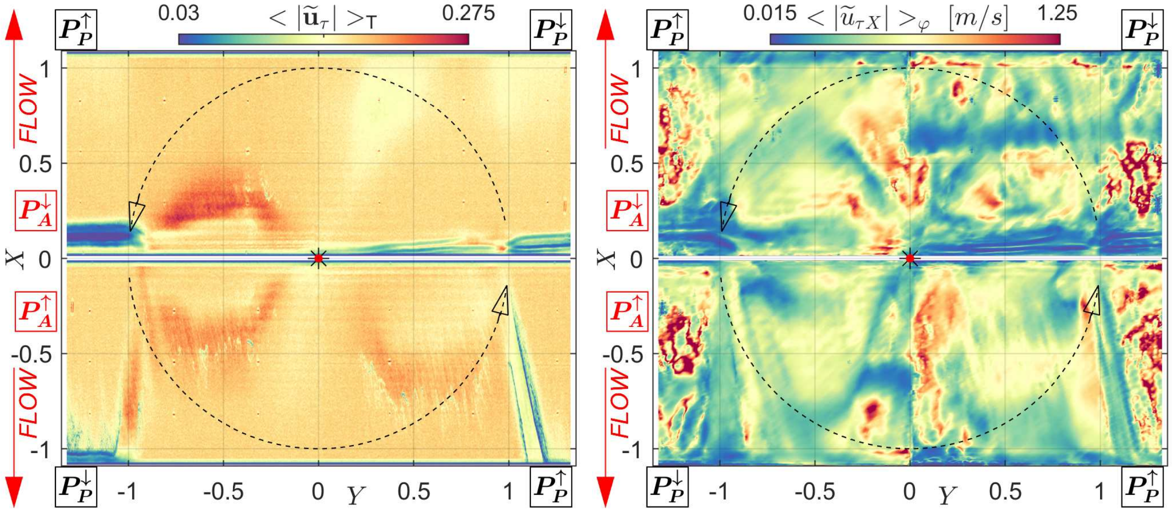

Figure 16: Modulus of time $\langle|\boldsymbol{u}_\tau|\rangle_\mathsf{T}$ (left) and ensemble average of phase-averaged friction velocity streamwise component $\langle|\widetilde{u}_{\tau X}|\rangle_\varphi$ (right) evaluated with TH algorithm at $AoA = 8°$. Black arrows on right side mark the signature of the tip vortex ($\mathbb{T}$) passage.

dimensional LSB even inside the streamtube, as shown by the skin-friction topology in Figure 13. Instantaneous maps of phase averaged temperature $\widetilde{T}$ and $\widetilde{\boldsymbol{\tau}}/|\tau|_{max}$ for the case at $AoA = 8°$ are presented in Figure 17 and exemplarily show a snapshot of the evolving complex interaction between manifolds at a specific phase angle ($\varphi = 212°$). The evolution of the manifold $\mathbb{L}$ inside the propeller streamtube, due to the interaction with the $\mathbb{W}$ manifold, is discussed in Sec. 5.4. In any case, the tendencies are similar to those observed outside of the streamtube.

5.3. Tip vortex and manifold $\mathbb{T}$

The second manifold described hereafter is associated with the tip vortex ($\mathbb{T}$ in Figure 1. Its striking features, observed in the $\langle|u_{\tau X}|\rangle_\varphi$-maps of Figures 14, 15 and 16 (right), are narrow, elongated strips with high $\langle|u_{\tau X}|\rangle_\varphi$, starting at $Y \approx \pm 1$ on the leading edge, which are oriented in the streamwise direction with a small angle with respect to the freestream (black arrows in the figures). These strips are the signatures of intense vortical structures generated at the tip of the blades. The tip vortices approach the model leading edge at $Y \approx \pm 1$, deform by stretching in the streamwise direction, and induce high skin friction in the aforementioned strips. They are coupled to more energetic structures connecting the region where $\mathbb{T}$ impacts on the model leading edge to the $\mathbb{L}$ outside of the propeller streamtube. These latter structures leads to the L-shaped regions of high σ_T in Figures 8 (right) and 9. At this point, it should be emphasized that this description is related only to the effect of $\mathbb{T}$ on σ_T and $\langle|u_{\tau X}|\rangle_\varphi$ and will be enriched by the skin-friction topologies at different phase angles presented in the next section (Sec. 5.4).

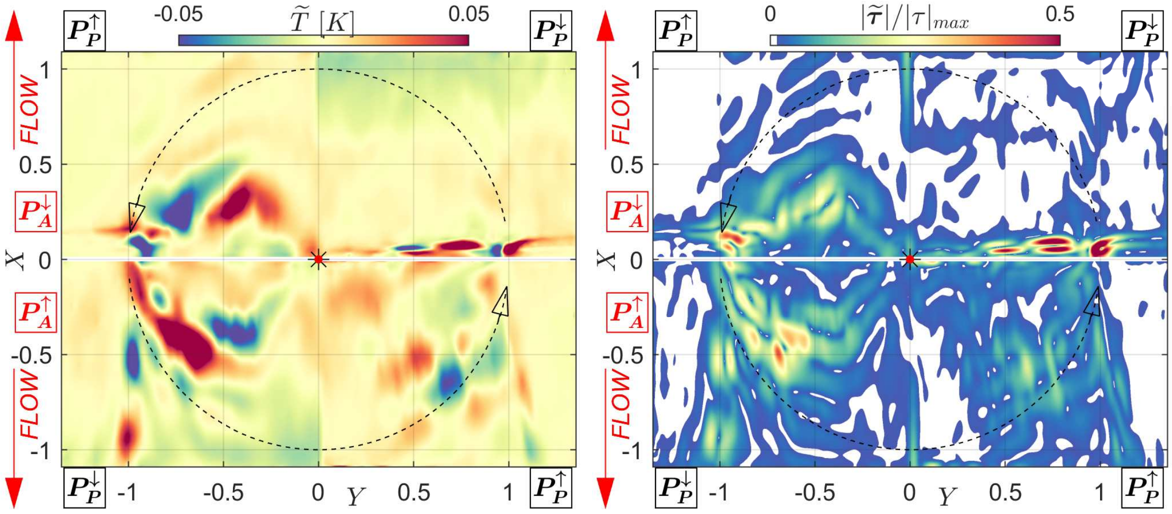

Figure 17: Temperature (left) and $|\boldsymbol{\tau}|/|\tau|_{max}$ (right) maps at phase instant $\varphi = 212°$, $AoA = 8°$. Clues about the simultaneous presence of the tip $\mathbb{T}$ and deformed LSB $\mathbb{L}$ are visible in the $|\boldsymbol{\tau}|/|\tau|_{max}$ map near the trailing edge, as slightly diverging couples of parallel traces. Separation appears at $[P_A^{\downarrow} P_P^{\downarrow}]$ and $[P_A^{\downarrow} P_P^{\uparrow}]$, close to the trailing edge.

5.4. Blades wake and manifold $\mathbb{W}$

The third manifold investigated and described in what follows represents the fingerprint of the vortex sheet generated and released by the blade trailing edge (manifold $\mathbb{W}$ in Figure 1). The wake released at each passage of the blade trailing edge propagates downstream and interacts with the hydrofoil (see e.g. Okulov and Sórensen, 2010; Felli et al., 2009). Here we focus on few macroscopic features by describing phenomena occurring at $AoA = 0°$ in the quadrant $[P_A^{\updownarrow} P_P^{\downarrow}]$, which are analyzed on the basis of the relative skin-friction fields obtained via the OF algorithm. The skin-friction topologies at the four different, equispaced phase angles $\varphi = [84°, 100°, 116°$ and $132°]$ are shown in Figures 18A B, C and D, respectively. They are superimposed over the magnitude of the streamwise and spanwise component of the relative skin friction $\widetilde{\tau}_X/\widetilde{\tau}_{Xref}$ and $\widetilde{\tau}_Y/\widetilde{\tau}_{Yref}$ in the left and right columns of Figure 18, respectively. The corresponding figures are indicated by the subscript $_X$ and $_Y$, respectively. The curvature of $\mathbb{W}$ causes the first interaction between the manifold and the leading edge to occur at $Y \approx 0.22$: the oblique orientation angle of the blade vortex sheet induces a disturbance in the skin-friction field propagating with both positive velocity components (Figure 18A) and deforming accordingly. Figure 18B shows $\mathbb{W}$ protruding downstream with non-uniform fiction velocity components, while counteracted by the adverse pressure gradient on the hydrofoil surface (which is enhanced by the propeller-induced under-pressure). At a phase lag $\Delta\varphi = 32°$, the tip vortex of the manifold $\mathbb{W}$ (manifold $\mathbb{T}$) reaches the hydrofoil leading edge and starts to interact with the hydrofoil surface. The spiral node in Figure $18C_Y$ at $Y \approx 0.85$ captures the $\mathbb{T}$ fingerprint and its stretch on the hydrofoil surface. It rises a wash-up/wash-down signature that elongates downstream although

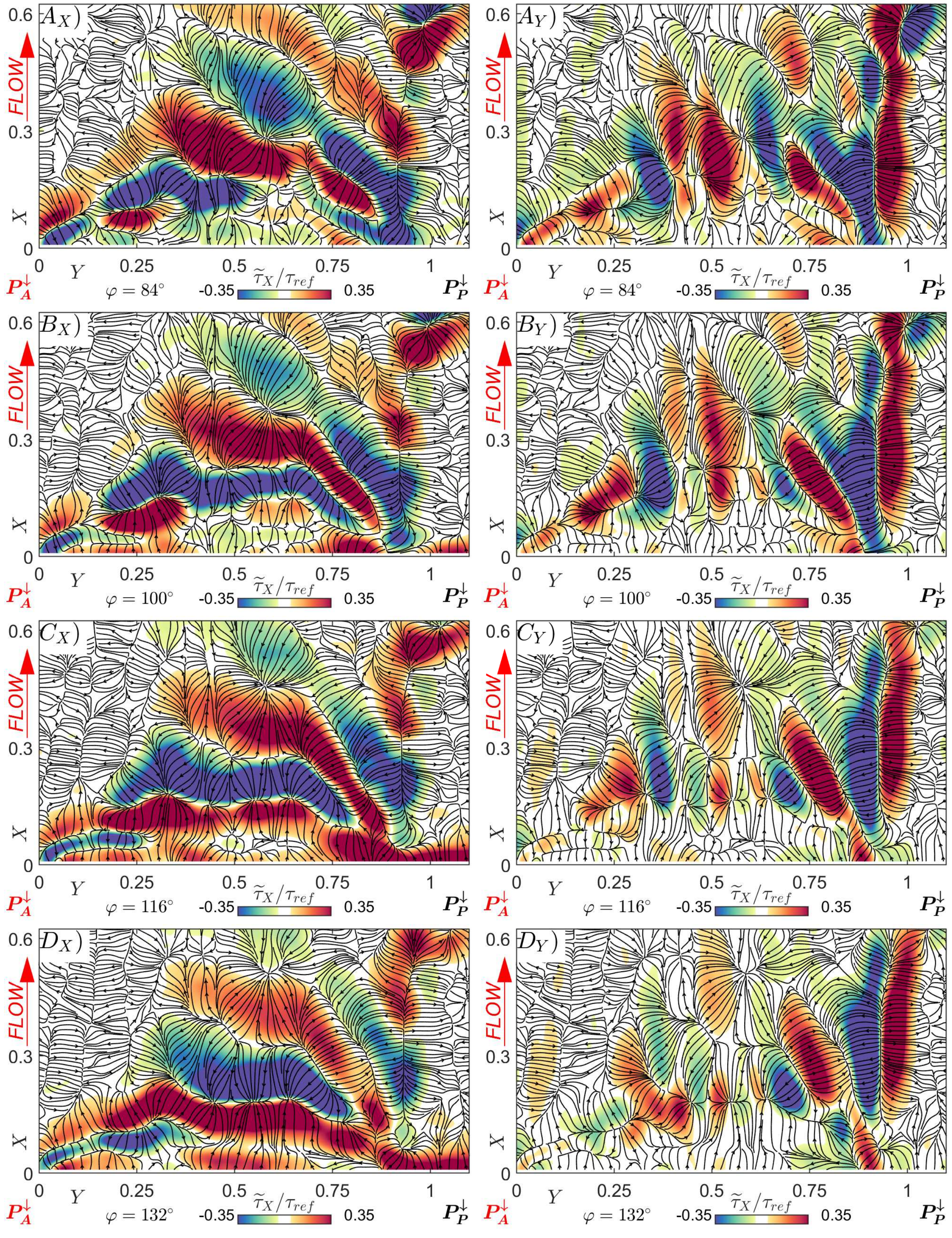

Figure 18: Topology of $\boldsymbol{\tau}$ vector field overlapped to $\widetilde{\tau}_X/\widetilde{\tau}_{Xref}$ and $\widetilde{\tau}_Y/\widetilde{\tau}_{Yref}$ at equispaced phase instants $\varphi = [84°, 100°, 116°, 132°]$ in the quadrant $[P_A^{\downarrow} P_P^{\downarrow}]$ at $AoA = 0°$. The stretch of the color scale saturates some regions, but makes the graph more readable.

maintaining, at least for the first instants after the contact with the hydrofoil model (up to $\varphi = 132°$), a topological continuity with the blade wake signature (see Figures 18C-D).

It is worth noting that the streamwise evolution of the $\mathbb{T}$ signature at $[P_A^{\downarrow} P_P^{\downarrow}]$ is strictly paired with the coherent structure resulting from the deformation of the LSB but, due to the force of its image-vortex, follows the opposite spanwise direction (Figure 14, 15, 16, right). Their coupling ceases at $X \approx 0.6$, i.e. in correspondence with the residual LSB ($\mathbb{L}$) outside of the propeller streamtube (see Sec. 5.2), because of the tip vortex break down probably induced by the adverse pressure gradient. Further downstream, $\mathbb{T}$ reconnects to its counterpart on the opposite hydrofoil surface and to continue its evolution towards the trailing edge (Felli et al., 2009). Except for the case at $AoA = 8°$, $P_A^{\downarrow}$, where no evidence of this development is found, all other configurations report $\mathbb{T}$ traces to extend from the leading to the trailing edge, but further information about breakdown and reconnection requires additional investigation. It could be conjectured that such breakdown of the tip occurs at an appreciable distance from the wall, and therefore it does not imprint a specific signature on temperature and skin-friction fields on the hydrofoil surface.

5.5. Propeller hub and manifold $\mathbb{H}$

The energetic vortex $\mathbb{H}$ that rises from the propeller hub features an opposite spin with respect to the tip vortex $\mathbb{T}$. Because of its interaction with the hydrofoil surfaces, its path (and that of the associated image vortex) is deflected, in the direction opposite to $\mathbb{T}$. This behavior is documented in Figure 19, which reports the spanwise component of $\boldsymbol{u}_\tau$ and thus reveals the associated $\mathbb{H}$ trace. This result, obtained with the still under-development TR algorithm (see Sec. 4.1.2), underlines the capability of the novel approach to capture a portrait of the thermal blobs displacement with cogent accuracy.

5.6. Separation at trailing edge and manifold $\mathbb{S}$

The last manifold we consider in this paper is the one generating at trailing edge (manifold $\mathbb{S}$ in Figure 1), where traces of flow separation appear at specific phase instants, in the $[P_A^{\downarrow} P_P^{\downarrow}]$ quadrant, as in the case at $\varphi = 212°$ shownn in Figure 17. This suggestion is quantitatively confirmed by the strip of $|\langle \tilde{u}_{\tau X} \rangle_\mathrm{T}| \to 0$ that can be seen at $X \approx 0.55$ in Figure 16 (right). The interested reader can gain a more specific idea of the phase averaged flow behavior by looking at the movies of $\widetilde{T}$ and $|\widetilde{\boldsymbol{\tau}}|$ attached as additional material to the present manuscript.

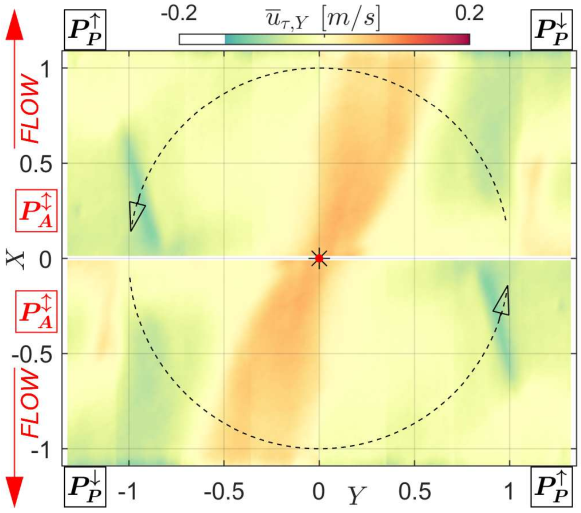

Figure 19: Streamwise $\overline{u}_{\tau Y}$ component at $AoA = 0^\circ$ evaluated with TR algorithm. The $\overline{u}_{\tau Y}$ signature marks the vortex deflection opposite to the propeller spin. Close to $Y \approx \pm 1$ a coherent structure appears on both $[P_P^{\uparrow}]$ and $[P_P^{\downarrow}]$ quadrants, marking the stretched $\mathbb{L}$ extension. The rotation of such a coherent structure is opposite to the inward one that marks the passage of the tip vortex $\mathbb{T}$, just visible on $P_P^{\downarrow}$ quadrant.

5.7. *Proper Orthogonal Decomposition and characteristic frequencies of phase evolution*

The description of the flow structures reported so far considers the various manifolds as isolated features evolving around the hydrofoil, providing a more detailed representation of their interaction only for the blade wake $\mathbb{W}$ (Section 5.4). The Proper Orthogonal Decomposition (POD) appears as an appropriate tool for a deeper understanding of the investigated phenomena, since the manifolds can be associated with a characteristic temporal behavior and a specific spatial localization. It allows the identification of the reciprocal correlation between the flow features and provides an accurate description of their time evolution by extracting the most correlated spatial modes $\mathbf{\Psi}_k(\mathbf{x})$ associated with specific time coefficients $\lambda_k(t)$, which represent the weight of k mode with respect to the overall dataset time by time. It is well known that the POD decomposition, here implemented following the *snapshot* criteria described in Sirovich (1987), is able to optimize the following form:

$$f(\mathbf{x}, t) = \sum_{k=1}^{M} \lambda_k(t) \mathbf{\Psi}_k(\mathbf{x}) \tag{18}$$

by identifying the $\mathbf{\Psi}_k(\mathbf{x})$ eigenmodes as the most correlated ones with the original data field, i.e. those that retain the maximum energy amount. The $\lambda_k(t)$ time coefficients, representing the inner product between the k^{th} eigenmode and the data field at time t, are the ideal candidates to extract information about a periodic behavior partially hidden in a noisy background, like in TSP temperature maps.

Figure 20 summarizes the results of the decomposition applied to phase averaged series

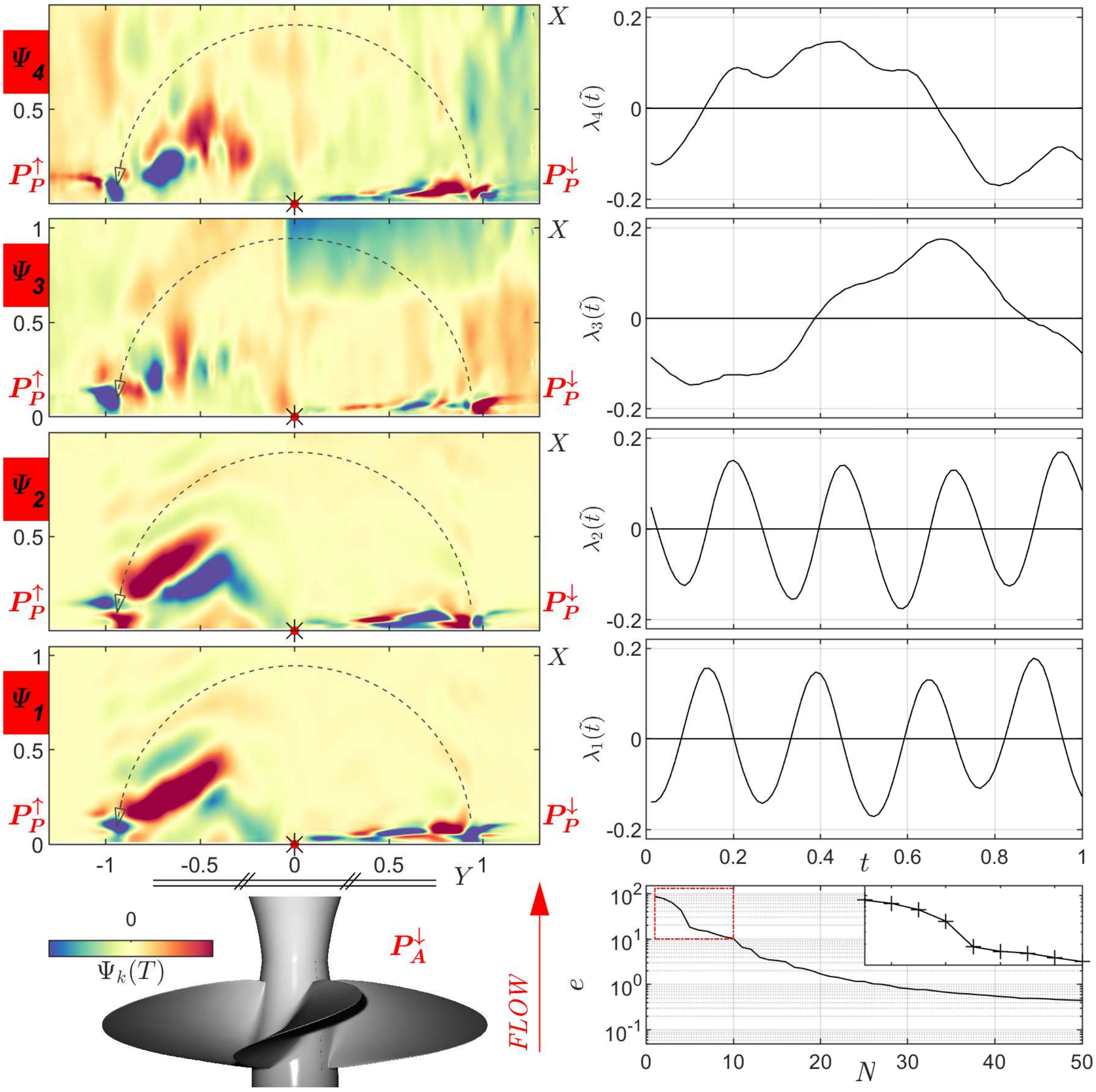

Figure 20: Proper Orthogonal Decomposition of $\widetilde{T}$ on the hydrofoil suction surface ($P_A^{\downarrow}$) at $AoA = 8°$: first four modes $\mathbf{\Psi}_{1-4}(\mathbf{x})$ (left) and the corresponding time coefficients $\lambda_{1-4}(t)$ (right). Lowest rightmost graph reports the spectrum of the eigenvalues e and a detail of the energy decay of the first 10 modes. Flow is from the bottom.

of temperature $\widetilde{T}$. $\widetilde{T}$ most energetic modes pulse with non-dimensional frequency of 4 (modes $\mathbf{\Psi}_1(\mathbf{x})$ and $\mathbf{\Psi}_2(\mathbf{x})$) or 1 (modes $\mathbf{\Psi}_3(\mathbf{x})$ and $\mathbf{\Psi}_4(\mathbf{x})$), as shown by their associated time coefficients $\lambda_{1-4}(t)$. Modes $\mathbf{\Psi}_1(\mathbf{x})$ and $\mathbf{\Psi}_2(\mathbf{x})$ capture phenomena related to the blades wake, emphasizing the previously described squeezing of the manifolds $\mathbb{W}$ and $\mathbb{L}$ against the leading edge in the $[P_A^{\downarrow} P_P^{\downarrow}]$ quadrant and deforming of $\mathbb{W}$ on the opposite half side $[P_A^{\downarrow} P_A^{\uparrow}]$. The dynamics revealed by modes $\mathbf{\Psi}_3(\mathbf{x})$ and $\mathbf{\Psi}_4(\mathbf{x})$ concerns the alternation of warmer and colder spots along *loci* corresponding to separation lines (see Sec. 5.2). This kind of temperature distribution is found to correspond to a sequence of converging nodes connected by saddle points (Miozzi et al., 2019), i.e. to the signature of a $3D$ separation, as introduced in Surana et al. (2006). The same modes also capture a dynamics probably attributable to a separation at the trailing edge occurring in the $[P_A^{\downarrow} P_P^{\downarrow}]$ quadrant. In particular, the large colder region close to the trailing edge in $\mathbf{\Psi}_3(\mathbf{x})$ allows to conjecture a colder water intrusion due to separation and recirculating turbulent flow during positive $\lambda_3(t)$ period (see the corresponding strip of $|\langle|u_{\tau X}|\rangle_{\mathrm{T}}| \rightarrow 0$ in Figure 16 (right)).

The weak contribution of the hub vortex $\mathbb{H}$ to the POD modes is likely due to the trumpet-shaped hub configuration adopted in the present work, which reduces the hub vortex instability, this resulting in an almost steady signature not visible by the POD decomposition.

6. Conclusion and further developments

We report about the application of TSP to the measurement of the non-uniform, unsteady flow around a hydrofoil immersed in a propeller wake. The interest in such an approach mainly relies upon the availability of temperature data to feed algorithms estimating qualitative and quantitative skin-friction fields. The three methods here described, named OF, TH, and TR algorithm, ground on different backgrounds, namely the energy equation at the wall and the passive transport equations, and feature strength and weakness requiring a critical application. As an example, the hard-to-impose uniform heat flux boundary condition enforces the TSP signal-to-noise ratio but, at the same time, introduces a bias in the time-averaged temperature obtained in the present work because of the adopted heating-system architecture. The restrictions imposed by this bias on the applicability of the OF algorithm (Liu and Woodiga, 2011), suggest the introduction of methods relying on temperature disturbance transport, thus ignoring the time-averaged field. The suggestion in (Geng et al., 2015) drives the development of the TH algorithm. It relies on a maximum-likelihood condition between the celerity of propagation of temperature disturbances and the velocity of propagation of a temperature wave as prescribed by the Taylor hypothesis. The novel TR algorithm heads towards the direction suggested by (Kim and Hussain, 1993), concerning the estimation of the displacement of thermal disturbances using a correlation measurement, and reprised in Miozzi et al. (2019) using temperature data. The approach is expanded in this work by adopting a classical optical-flow evaluation of the temperature motion field from couples of successive instantaneous temperature maps, and preliminary results obtained with the so-designed TR algorithm encourage further development.

The complex and challenging propeller wake flow becomes even more complicated when interacting with a lifting hydrofoil surface. The presence of a more or less intense, incidence-induced adverse pressure gradient on the hydrofoil surface, altered by the propeller-induced over- and under-pressure contribution, displaces the LSB from its natural position (i.e. the position on the isolated hydrofoil at the same Re and AoA) and determines the degree of penetration of the tip vortex and the blade wake before

their breakdown. The proposed approach considers two classes of flow manifolds: one class originating at the propeller stage (blade trailing edge $\mathbb{W}$ and blade tip $\mathbb{T}$, hub $\mathbb{H}$), and the other class taking place at the hydrofoil stage (laminar separation bubble $\mathbb{L}$ and trailing-edge separation $\mathbb{S}$). The periodicity of the flow allows adopting the triple Reynolds decomposition of both temperature T and skin-friction $\boldsymbol{\tau}$ fields at the wall; each term of the decomposition (time-average, periodic contribution and random component) provides useful insights in the flow features.
In more detail, the reported results unveil the influence of the incidence-induced adverse pressure gradient in defining a spatial organization of the time-averaged flow on the hydrofoil surface, being the LSB a well-marked placeholder. The phase-averaged analysis allows showing the cutting of a blade wake operated by the hydrofoil model and suggests the existence of a still unexplored potential relying on the TSP approach.

Acknowledgments

This work has been supported by the Flagship Project RITMARE, The Italian Research for the Sea, coordinated by the Italian National Research Council and funded by the Italian Ministry of Education, University and Research. Dr. Christian Klein (DLR) is acknowledged for his organizational and logistic support, and also for the application of the TSP to the hydrofoil model. Carsten Fuchs (DLR) is acknowledged for TSP surface treatment. Dr. Alessandro Capone (CNR-INM) is acknowledged for his contribution during setup design. Dr. Fabio Di Felice (CNR-INM) is acknowledged for the organizational and logistic support.

References

Adrian, R.J., 2007. Hairpin vortex organization in wall turbulencea. Physics of Fluids 19.

Baker, S., Matthews, I., 2004. Lucas-Kanade 20 years on: A unifying framework. International Journal of Computer Vision 56, 221–255. doi:`doi.org/10.1023/B:VISI.0000011205.11775.fd`.

Benzi, R., Sutera, A., Vulpiani, A., 1981. The mechanism of stochastic resonance. Journal of Physics A: Mathematical and General 14, L453–L457. doi:`10.1088/0305-4470/14/11/006`.

Capone, A., Klein, C., Di Felice, F., Beifuss, U., Miozzi, M., 2015. Fast-response underwater TSP investigation of subcritical instabilities of a cylinder in crossflow. Experiments in Fluids 56, 1–14.

Costantini, M., 2016. Experimental analysis of geometric, pressure gradient and surface temperature effects on boundary-layer transition in compressible high Reynolds number flows. PhD Thesis, RWTH Aachen.

Costantini, M., Fey, U., Henne, U., Klein, C., 2015. Nonadiabatic surface effects on transition measurements using temperature-sensitive paints. AIAA Journal 53, 1172–1187.

Costantini, M., Fuchs, C., Henne, U., Klein, C., Ondrus, V., Bruse, M., Löhr, M., Jacobs, M., 2019. Experimental analysis of a wind-turbine rotor blade airfoil by means of Temperature-Sensitive Paint, in: AIAA 2019 Scitech Forum, pp. 2019–0800.

Costantini, M., Hein, S., Henne, U., Klein, C., Koch, S., Schojda, L., Ondrus, V., Schröder, W., 2016. Pressure gradient and non-adiabatic surface effects on boundary-layer transition. AIAA Journal 54, 3465–3480.

Del Álamo, J.C., Jiménez, J., 2009. Estimation of turbulent convection velocities and corrections to Taylor's approximation. Journal of Fluid Mechanics 640, 5–26.

Délery, J., 2013. Three-dimensional separated flows topology: Singular points, beam splitters and vortex structures. Focus series in fluid mechanics, John Wiley & Sons, Ltd. doi:`10.1002/9781118578544.ch2`.

Dodda, A., Oberoi, A., Sebastian, A., Choudhury, T.H., Redwing, J.M., Das, S., 2020. Stochastic resonance in mos2 photodetector. Nature Communications 11.

Eckelmann, H., 1974. The structure of the viscous sublayer and the adjacent wall region in a turbulent channel flow. Journal of Fluid Mechanics 65, 439–459.

Felli, M., 2021. Underlying mechanisms of propeller wake interaction with a wing. Journal of Fluid Mechanics 11, A10.

Felli, M., Camussi, R., Guj, G., 2009. Experimental analysis of the flow field around a propeller-rudder configuration. Experiments in Fluids 46, 147–164.

Fey, U., Engler, R.H., Egami, Y., Iijima, Y., Asai, K., Jansen, U., Quest, J., 2003. Transition detection by temperature sensitive paint at cryogenic temperatures in the European Transonic Wind tunnel (ETW), in: ICIASF Record, International Congress on Instrumentation in Aerospace Simulation Facilities, pp. 77–88.

Gardner, A.D., Richter, K., 2015. Boundary layer transition determination for periodic and static flows using phase-averaged pressure data. Experiments in Fluids 56.

Gaster, M., 1966. The structure and behavior of laminar separation bubbles. AGARD CP-4 , 813–854.

Geng, C., He, G., Wang, Y., Xu, C., Lozano-Durán, A., Wallace, J.M., 2015. Taylor's hypothesis in turbulent channel flow considered using a transport equation analysis. Physics of Fluids 27, 025111.

Hetsroni, G., Tiselj, I., Bergant, R., Mosyak, A., Pogrebnyak, E., 2004. Convection velocity of temperature fluctuations in a turbulent flume. Journal of Heat Transfer 126, 843–848.

Hirschel, E.H., Kordulla, W., Cousteix, J., 2014. Three-dimensional attached viscous flow: Basic principles and theoretical foundations. Springer-Verlag Berlin Heidelberg. doi:`10.1007/978-3-642-41378-0`.

Horn, B.K., Schunck, B.G., 1981. Determining optical flow, in: 1981 Technical symposium east, International Society for Optics and Photonics. pp. 319–331.

Hosseini, M.S., Plataniotis, K.N., 2017. Finite differences in forward and inverse imaging problems: Maxpol design. SIAM Journal on Imaging Sciences 10, 1963–1996.

Jiménez, J., 2018. Coherent structures in wall-bounded turbulence. Journal of Fluid Mechanics 842, P1.

Johansson, A.V., Alfredsson, P.H., Kim, J., 1991. Evolution and dynamics of shear-layer structures in near-wall turbulence. Journal of Fluid Mechanics 224, 579–599.

Kim, J., Hussain, F., 1993. Propagation velocity of perturbations in turbulent channel flow. Physics of Fluids A 5, 695–706.

Koenderink, J.J., 1984. The structure of images. Biological cybernetics 50, 363–370.

Kroeger, T., Timofte, R., Dai, D., Van Gool, L., 2016. Fast optical flow using dense inverse search, in: Leibe, B., Matas, J., Sebe, N., Welling, M. (Eds.), Computer Vision – ECCV 2016, Springer International Publishing. pp. 471–488. doi:`doi.org/10.1007/978-3-319-46493-0_29`.

Lighthill, M., 1963. Attachment and separation in three-dimensional flow. Laminar boundary layers 2, 72–82.

Liu, T., 2013. Extraction of skin-friction fields from surface flow visualizations as an inverse problem. Measurement Science and Technology 24, 124004.

Liu, T., Sullivan, J.P., 2005. Pressure-and Temperature-Sensitive Paints. Springer.

Liu, T., Woodiga, S., 2011. Feasibility of global skin friction diagnostics using temperature sensitive paint. Measurement Science and Technology 22, 115402.

Lucas, B.D., Kanade, T., 1981. An iterative image registration technique with an application to stereo vision, in: Proceedings of the 7th International Joint Conference on Artificial Intelligence - Volume 2, Morgan Kaufmann Publishers Inc., San Francisco, CA, USA. p. 674–679.

Miozzi, M., Capone, A., Costantini, M., Fratto, L., Klein, C., Di Felice, F., 2019. Skin friction and coherent structures within a laminar separation bubble. Experiments in Fluids 60, 13.

Miozzi, M., Capone, A., Di Felice, F., Klein, C., Liu, T., 2016. Global and local skin friction diagnostics from TSP surface patterns on an underwater cylinder in crossflow. Physics of Fluids 28, 124101.

Miozzi, M., Capone, A., Klein, C., Costantini, M., 2020a. Incipient stall characterization from skin-friction maps. International Journal of Numerical Methods for Heat and Fluid Flow .

Miozzi, M., Di Felice, F., Klein, C., Costantini, M., 2020b. Taylor hypothesis applied to direct measurement of skin friction using data from temperature sensitive paint. Experimental Thermal and Fluid Science 110, 109913.

Muscari, R., Dubbioso, G., Di Mascio, A., 2017. Analysis of the flow field around a rudder in the wake of a simplified marine propeller. Journal of Fluid Mechanics 814, 547–569. doi:`10.1017/jfm.2017.43`.

Okulov, V.L., Sórensen, J.N., 2010. Applications of 2d helical vortex dynamics. Theoretical and Computational Fluid Dynamics 24, 395–401.

Ondrus, V., Meier, R., Klein, C., Henne, U., Schäferling, M., Beifuss, U., 2015. Europium 1,3-di(thienyl)propane-1,3-diones with outstanding properties for temperature sensing. Sensors and Actuators A: Physical 233, 434 – 441. doi:`http://dx.doi.org/10.1016/j.sna.2015.07.023`.

Posa, A., Broglia, R., Balaras, E., 2020. Flow over a hydrofoil in the wake of a propeller. Computers & Fluids 213, 104714. doi:`https://doi.org/10.1016/j.compfluid.2020.104714`.

Reynolds, W.C., Hussain, A.K.M.F., 1972. The mechanics of an organized wave in turbulent shear flow. Part 3. Theoretical models and comparisons with experiments. Journal of Fluid Mechanics 54, 263–288. doi:`10.1017/S0022112072000679`.

Risius, S., Costantini, M., Koch, S., Hein, S., Klein, C., 2018. Unit Reynolds number, Mach number and pressure gradient effects on laminar–turbulent transition in two-dimensional boundary layers. Experiments in fluids 59, 29.

Salvatore, F., Pereira, F., Felli, M., Calcagni, D., Di Felice, F., 2006. Description of the INSEAN E779A propeller experimental dataset. Technical Report INSEAN 2006-085. INSEAN-Italian Ship Model Basin.

Schafer, R.W., 2011. What is a Savitzky-Golay filter? IEEE Signal Processing Magazine 28, 111–117.

Sirovich, L., 1987. Turbulence and the dynamics of coherent structures. I - Coherent structures. II - Symmetries and transformations. III - Dynamics and scaling. Quarterly of Applied Mathematics 45, 561–571.

Surana, A., Grunberg, O., Haller, G., 2006. Exact theory of three-dimensional flow separation. Part 1. Steady separation. Journal of fluid mechanics 564, 57–103.

Tropea, C., Yarin, A.L., Foss, J.F., 2007. Springer handbook of experimental fluid mechanics. Springer Science & Business Media.